IRON-DEPENDENT CELLULAR REPROGRAMMING OF MIXED SUBSTRATE METABOLISM IN *PSEUDOMONAS PUTIDA* KT2440

A Thesis

Presented to the Faculty of the Graduate School

Of Cornell University

In Partial Fulfillment of the Requirements for the Degree of

Master of Engineering

By

Caroll Michelle Mendonca

May 2017

ABSTRACT

We investigated the consequences of Fe-limitation on the metabolism of mixed organic substrates. The following study presents a stable isotope-assisted metabolomics approach using ^{13}C-labeled substrates and liquid chromatography-mass spectrometry (LC-MS) to evaluate the effects of Fe availability on co-utilization of glucose and benzoate in *P. putida* KT2440 cells. We provide new metabolic insights regarding nutrient dependent carbon metabolism of the biotechnologically important *Pseudomonas* species across three conditions: (1) Fe-replete condition, wherein the Fe concentration was within the optimal range for bacterial growth; (2) Fe-limited medium, in which no exogenous supply of Fe was provided; and (3), Fe-starved condition with ethylene-diamine-tetra-acetic-acid, a strong Fe chelator, in the growth a medium to evaluate the effects of very low Fe conditions. Our data revealed that Fe-limitation did not have any effect on the biomass growth of the cells but there was an overall increase in substrate consumption accompanied by secretion of the pyoverdine siderophore. Under the Fe starvation condition, there was a diauxic growth in which the cells first consumed benzoate in the growth phase and, upon benzoate depletion, the cells started consuming glucose in the second phase. Interestingly, pyoverdine secretion was enhanced during the benzoate consumption phase. These results thus demonstrate that the preferential intake of the aromatic substrate as a function of decreasing Fe availability was favorable to siderophore production. The present findings provide new insights into the metabolic underpinnings of nutrient-dependent carbon metabolism.

BIOGRAPHICAL SKETCH

Caroll Mendonca earned her Bachelor of Engineering degree with a concentration in biotechnology from Visvesvaraya Technological University, India, where she did her undergraduate research on the characterization of metal-tolerant bacteria for bioremediation. During her undergraduate career, she worked for three years with a non-profit organization targeting equitable outcomes for children in shelter homes. In the fall of 2016, she joined Cornell University's Biological and Environmental Engineering department to pursue her Master of Engineering degree under the supervision of her advisor, Dr. Ludmilla Aristilde.

ACKNOWLEDGEMENTS

The work presented here was made possible through the help and support from a number of people. First and foremost, I sincerely thank Dr. Ludmilla Aristilde for the opportunity to work in her lab, and for her unconditional guidance, support and mentorship throughout my work. I'd also like to thank all the members of the Aristilde lab for their friendship and encouragement. I especially thank Julie Wuschensky, Rebecca Wilkes and Tracy Youngster for all their collaborations. I particularly thank Mathew Kukurugya. This research would not be possible without all of his previous work and present collaboration. I further acknowledge Dr. Ivan Keresztes of the Cornell NMR Facility and Dr. Murray McBride of Soil and Crop Sciences for their wisdom and help towards this project.

I'd like to express my immense gratitude towards Dr. Jordan Cook, Ishwarya Venkatesh, Nakita Marbaniang and Mark Mendonca for their constant love and support throughout my M.Eng.

Finally, I thank my parents and best friends, Dr. Norman and Nancy Mendonca for their perpetual and irreplaceable love.

TABLE OF CONTENTS

Abstract……...iii

Biographical Sketch……iv

Acknowledgements……..v

Table of Contents……vi

List of Figures……vii

List of Tables……..…ix

List of Abbreviations……..…….x

Introduction…….……..……..…..……1

Materials and methods…….……...……...……5

Result and Discussion

Growth Phenotype and Substrate Consumption……10

Fe-dependent substrate incorporation……13

Metabolic network structure……..……...……..……21

Siderophore Production…….37

Metabolic Flux Analysis…….……39

Concluding Remarks……..46

Bibliography……...……..……...……..48

Appendix……...…….……51

LIST OF FIGURES

Figure 1: Schematic representation of central carbon metabolism……..4

Figure 2: Growth curves for *P. putida* KT2440 cells grown on Fe-replete, Fe-limited and Fe-starved glucose-benzoate mixture.……11

Figure 3: Growth rates (h^{-1}) for *P. putida* KT2440 cells grown on glucose-benzoate mixture during Fe-replete (Kukurugya, 2017), Fe-limited and Fe-starved conditions…….....……12

Figure 4: Consumption of glucose and benzoate for *P. putida* KT2440 cells grown on Fe-replete (Kukurugya, 2017), Fe-limited and Fe-starved glucose-benzoate mixture…….…..12

Figure 5: Carbon equivalent consumption rates (mmol C $gCDW^{-1}$ h^{-1}) for *P. putida* KT2440 cells grown on Fe-replete (Kukurugya, 2017), Fe-limited and Fe-starved glucose-benzoate mixture…….……..……13

Figure 6: Schematic representation of ^{13}C-labeled metabolites in ED and reverse EMP pathways when grown on [U-$^{13}C_6$]-glucose and unlabeled benzoate……...……..…….15

Figure 7: Labeling of the ED and reverse EMP pathway metabolites in pseudo-steady state at optical density (OD_{600}) 0.4 in Fe-limited and Fe-starved cells; 0.5 Fe-replete cells when grown on [U-$^{13}C_6$]-glucose and unlabeled benzoate…...…….…16

Figure 8: Schematic representation of ^{13}C-labeled metabolites in central carbon metabolism when grown on [U-$^{13}C_6$]-glucose and unlabeled benzoate in reverse EMP pathway and TCA cycle……...18

Figure 9: Labeling of the TCA cycle metabolites in pseudo-steady state at optical density (OD_{600}) 0.4 in Fe-limited and Fe-starved cells and 0.5 Fe-replete cells when grown on [U-$^{13}C_6$]-glucose and unlabeled benzoate …….....…19

Figure 10: Labeling of the PP metabolites in pseudo-steady state at optical density (OD_{600}) 0.4 in Fe-limited and Fe-starved cells and 0.5 Fe-replete cells when grown on [U-$^{13}C_6$]-glucose and unlabeled benzoate …….....…20

Figure 11: Schematic representation of ^{13}C-labeled metabolites in in ED and reverse EMP pathways during growth on [1,5,6-$^{13}C_3$]-glucose and unlabeled benzoate. …….....……24

Figure 12: The isotopic labeling fractions, with standard deviations, for intracellular metabolites in the ED and EMP pathways when grown on [1,5,6-$^{13}C_3$]-glucose and unlabeled benzoate under Fe-limitation at $O.D_{600}$ 0.4 and 0.8. …….....……...……25

Figure 13: The isotopic labeling fractions, with standard deviations, for intracellular metabolites in the ED and EMP pathways when grown on [1,5,6-$^{13}C_3$]-glucose and unlabeled benzoate under phase 1 Fe-starvation at $O.D_{600}$ 0.4 and 0.8.…….....….....26

Figure 14: The isotopic labeling fractions, with standard deviations, for intracellular metabolites in the ED and EMP pathways when grown on [1,5,6-$^{13}C_3$]-glucose and unlabeled benzoate under phase 2 Fe-starvation at $O.D_{600}$ 0.4 and 0.8. ..……..……...…..…….....27

Figure 15: Schematic representation of ^{13}C-labeled metabolites in PP pathway when grown on [1,5,6-$^{13}C_3$]-glucose and unlabeled benzoate...……...……..29

Figure 16 : The isotopic labeling fractions, with standard deviations, for intracellular metabolites in the PP pathways when grown on [1,5,6-$^{13}C_3$]-glucose and unlabeled benzoate under Fe-limitation at $O.D_{600}$ 0.4 and 0.8. ..…….....……30

Figure 17: The isotopic labeling fractions, with standard deviations, for intracellular metabolites in the PP pathways when grown on [1,5,6-$^{13}C_3$]-glucose and unlabeled benzoate during first phase of Fe-starvation at $O.D_{600}$ 0.4 and 0.8. ..……...…….....30

Figure 18: The isotopic labeling fractions, with standard deviations, for intracellular metabolites in the PP pathways when grown on [1,5,6-$^{13}C_3$]-glucose and unlabeled benzoate during second phase of Fe-starvation at $O.D_{600}$ 0.4 and 0.8..…….....31

Figure 19:Schematic representation of ^{13}C-labeled metabolites in the TCA cycle when grown on [1,5,6-$^{13}C_3$]-glucose and unlabeled benzoate. (Kukurugya, 2017)…....……...33

Figure 20: The isotopic labeling fractions, with standard deviations, for eight intracellular metabolites in central carbon metabolism when grown on [1,5,6-$^{13}C_3$]-glucose and unlabeled benzoate under Fe-limitation at $O.D_{600}$ 0.4 and 0.8…….....…….34

Figure 21: The isotopic labeling fractions, with standard deviations, for eight intracellular metabolites in central carbon metabolism when grown on [1,5,6-$^{13}C_3$]-glucose and unlabeled benzoate during first phase of Fe-starvation at $O.D_{600}$ 0.4 and 0.8…..…….....35

Figure 22: The isotopic labeling fractions, with standard deviations, for eight intracellular metabolites in in central carbon metabolism when grown on [1,5,6-$^{13}C_3$]-glucose and unlabeled benzoate during second phase of Fe-starvation at $O.D_{600}$ 0.4 and 0.8. …….....36

Figure 23: Siderophore secretion rates……..38

Figure 24: Metabolic flux analysis……....41

LIST OF TABLES

Table 1: The MFA output of each metabolic reaction: the flux value, and the standard deviation of the flux value normalized to the composite consumption rate…….....…..26

Table 2: The absolute optimal flux values from the MFA in the units of (mmol g_{CDW}^{-1} h^{-1})….....28

LIST OF ABBREVIATIONS

G6P	Glucose-6-phosphate
F6P	Fructose-6-phosphate
FBP	Fructose-1,6-bisphosphate
DHAP	Dihydroxyacetone phosphate
GAP	Glyceraldehyde-3-phosphate
3-PG	3-phosphoglycerate
PEP	Phosphoenolpyruvate
Pyr	Pyruvate
AcCoA	Acetyl coenzyme A
S7P	Sedoheptulose-7-phosphate
R5P	Ribose-5-phosphate
Xu5P	Xylulose-5-phosphate
E4P	Erythrose-4-phosphate
OAA	Oxaloacetate
α-KG	α-ketoglutarate
Gln	Glutamine
Glucn	Gluconate
2-Keto-Glucn	2-ketogluconate
Ru5P	Ribulose-5-phosphate

1. INTRODUCTION

Due to the role of iron (Fe) as an important cofactor in metabolic enzymes, Fe is a vital micronutrient that is essential for carbon metabolism (Andrews et al., 2003; Miransari, 2013). However, under aerobic conditions, the bioavailability of Fe is significantly limited. This limitation is primarily due to the presence of Fe in forms of lower solubility, Fe oxides and hydroxides (Bronstein et al., 2008; Braun and Hantke, 2011). In response to Fe limitation, aerobic bacteria deploy strategies to manage carbon metabolism and promote Fe acquisition. One notable strategy is the biosynthesis and secretion of high-affinity Fe-chelating specialized compounds (or siderophores) and low-affinity Fe-binding organic acids (Andrews et al., 2003). The primary siderophore produced by *Pseudomonas* species are pyoverdines (PVDs), which are non-ribosomal peptidic compounds (Peek et al. 2012; Cézard et al. 2015). In addition to the peptide chain of variable length, PVDs contain a 2,3-diamino-6,7-dihydroxyquinoline chromophore, and a carboxylic acid (or amide) side chain (Wei and Aristilde, 2015). The biosynthesis of PVD requires carbon investment from several pathways in the central carbon metabolism. The peptide chain is made of amino acids primarily derived from the tricarboxylic acid (TCA) cycle. The Fe-binding moieties are synthesized from pentose-phosphate (PP) pathway and the TCA cycle (Hider and Kong, 2010) metabolites: the catecholate moiety is derived from chorismate, a precursor to aromatic amino acids that is synthesized by combining erythrose-4-phosphate, a PP pathway metabolite, and phosphoenolpyruvate (PEP), a metabolite upstream of the TCA cycle; the hydroxamate moiety is synthesized from α-ketoglutarate (α-KG), a TCA cycle metabolite (Hider and Kong, 2010; Sasnow et al., 2016) (Fig. 1). The side chain group, which is composed of dicarboxylic acids (succinic acid and malic acid) or their monoamide derivatives, are TCA cycle metabolites (Cézard et al. 2015). The biosynthesis of

PVD is a carbon-expensive endeavor that consumes metabolic precursors away from biomass growth. Therefore, of special interest is the consequences of Fe-dependent metabolism on substrate utilization.

Here we seek to elucidate the effects of Fe availability on mixed-substrate metabolism in the model soil bacterium *Pseudomonas putida* KT2440. We chose glucose and benzoate for the content of our substrate mixture due to their relevance to natural carbon processing, contaminant bioremediation, and conversion of organic wastes to biofuels. In addition to being a breakdown product of cellulosic materials, glucose is a common carbohydrate in plant secretions (López-Mondéjar et al., 2016). Benzoate is an important metabolic intermediate in the biodegradation of lignin and aromatic contaminants (Michalska et al., 2012; Sudarsan et al., 2014; Sudarsan et al., 2016). Using ^{13}C tracer experiments, Kukurugya (2017) has elucidated the co-metabolism of glucose and benzoate in Fe-replete *P. putida* cells and quantified the carbon fluxes throughout the metabolic network. The initial catabolism of glucose and benzoate follow distinct paths before converging into the TCA cycle. Glucose-derived carbons were primarily routed to the Entner-Doudoroff (ED) pathway, reverse Embden-Meyerhof-Parnas (EMP) pathway and the PP pathway, whereas benzoate-derived carbon was routed almost exclusively to the TCA cycle via the ortho-pathway (Kukurugya, 2017) (Fig 1). Previous work on mixed substrate (sugar with aromatic compound) metabolism in *Pseudomonas* species depicted both a lack of substrate preference (Cao et al., 2007; Duuren et al., 2012, Sudarsan et al., 2014; Kukurugya, 2017), and a diauxic growth profile wherein either glucose or the aromatic substrate was the preferred substrate (Basu et al., 2007; Karishma et al., 2016). It remains to be investigated the effect of Fe-limited metabolism on carbon utilization from substrate mixtures.

With respect to effects of Fe availability on the metabolism of a single substrate, a previous study of Fe-limited *P. putida* cells grown on glucose alone reported a seven-fold reduction in the biomass growth when compared with Fe-replete cells (Sasnow et al., 2016). Carbon investment towards intracellular metabolism was impaired due to significant excretion (up to 50% of the carbon uptake) of gluconate, an oxidized glucose metabolite (Sasnow et al., 2016). Despite the significant decrease in intracellular carbon assimilation, the glucose-grown Fe-limited cells exhibited an equal investment of consumed carbon towards biomass growth and the PVD siderophore secretion (Sasnow et al., 2016). Furthermore, compared to *P. putida* cells grown solely on glucose, it was reported that cells grown on benzyl alcohol (an aromatic substrate) alone had more than 2-fold increase in PVD secretion (Joshi et al., 2014). This enhanced PVD secretion was proposed to be due to the high Fe demand for Fe-depending oxygenases, which are required to catalyze the aromatic substrate (Joshi et al., 2014). The consequences of Fe-limitation on mixed substrate metabolism and PVD production have not been elucidated.

Using a stable isotope-assisted metabolomics approach with liquid chromatography-mass spectrometry (LC-MS), we investigate the following four hypotheses regarding the effects of Fe availability on co-utilization of glucose and benzoate in *P. putida* KT2440 cells.: (1) the total carbon uptake from both substrates, and the biomass growth will be significantly decreased in Fe-limited cells compared to Fe-replete cells; (2) carbon-investment from glucose will be compromised due to rerouted glucose catabolism to gluconate secretion in Fe-limited cells; (3) catabolism of benzoate-derived carbons will be favored in Fe-limited cells due to their direct investment into the TCA cycle metabolite precursors to enhance PVD biosynthesis; (4) the carbon fluxes through the metabolic network will be regulated to accommodate selective substrate utilization from the mixture. We provide new metabolic insights regarding nutrient

dependent carbon metabolism of the biotechnologically important *Pseudomonas* species across three conditions: (1) Fe-replete growth medium, wherein the Fe concentration in growth medium was within the optimal range for bacterial growth (Vasil et al., 1999; Kim et al., 2009); (2) Fe-limited growth, in which no exogenous supply of Fe was provided; and (3) Fe-starved condition with ethylene-diamine-tetra-acetic-acid (EDTA) in the growth medium, a strong Fe chelator to evaluate the effects of very low Fe conditions (Kim et al., 2009). With these findings, we contribute to an emerging framework in understanding nutrient limitation, carbon metabolism and their co-dependence.

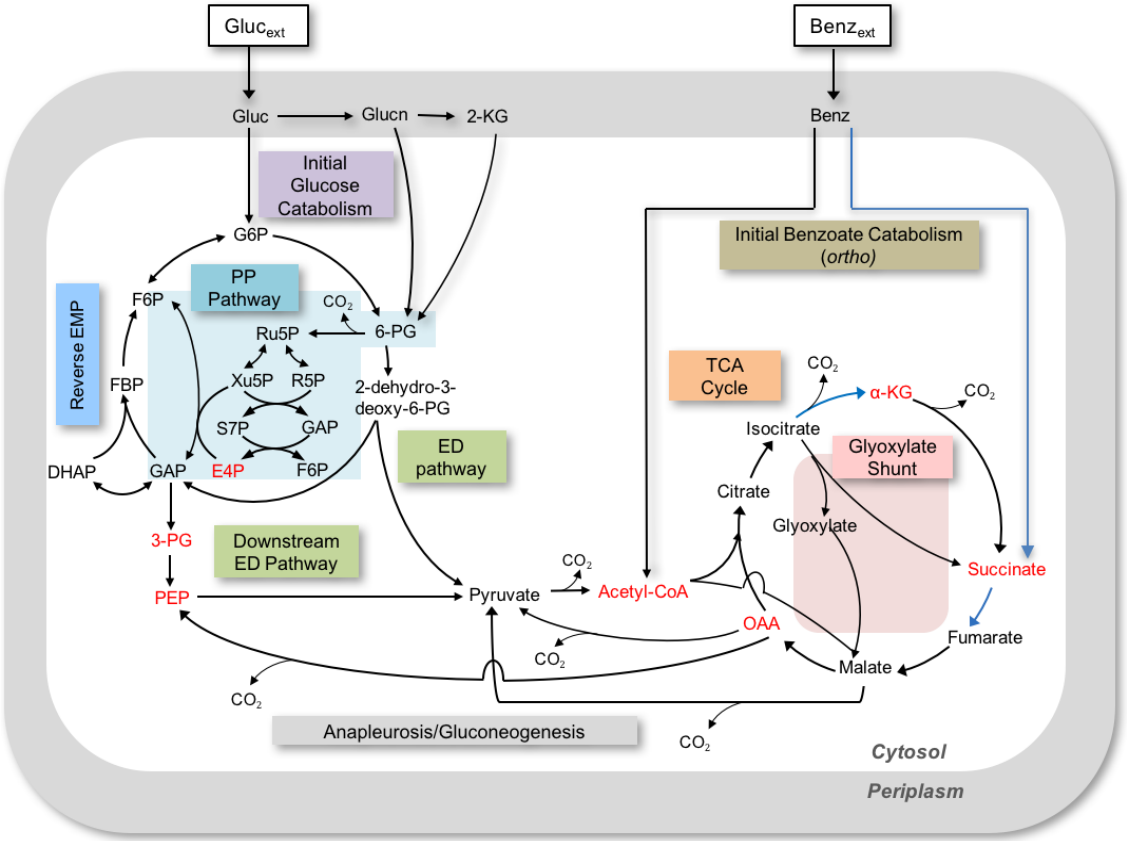

Fig.1: The metabolic routes through the Entner-Doudroff (ED) pathway, the pentose phosphate pathway (PPP), and the tricarboxylic acid (TCA) cycle are shown in black, the metabolites that are involved in siderophore biosynthesis are shown in red and the location of Fe-containing enzymes are shown in blue. Gluconate, Glucn; 2-ketogluconate, 2-keto-glucn; 6-phospho-gluconate, 6-PG; glucose-6-phosphate, G6P; fructose-6-phosphate, F6P; fructose-1,6-biphosphate, FBP; dihydroxyacetone-phosphate, DHAP; glyceraldehyde-3-phosphate, GAP; 3-phosphoglycerate, 3-PG; phosphoenolpyruvate, PEP; acetyl coenzyme A, A-coA; carbon dioxide, CO_2 (Figure courtesy of Dr. Ludmilla Aristilde, 2017).

2. MATERIALS AND METHODS

2.1 Culturing Conditions

Pseudomonas putida KT2440 was acquired from ATCC (American Type Culture Collection, Manassas, VA) as freeze-dried cultures and were plated on agar-solidified Luri-Bertani (LB) medium and stored at 4°C until use. The cells were re-suspended in LB medium as liquid cultures after selection of individual colonies from the plates. Liquid culturing was conducted in a G24 incubator shaker (New Brunswick Scientific, Edison, NJ) shaken at 220 rpm at 30°C in 250-mL baffled flasks. The volume of the suspended cells did not exceed 25-mL (i.e., one-tenth of total flask volume); the flasks were covered with sponge caps to enable gas exchange and prevent contamination.

The growth medium, which was filter-sterilized and pH-adjusted (pH 7.0) contained the following salts in Milli-Q water: 18.7 mM NH_4Cl, 0.81 mM $MgSO_4$, 34 µM $CaCl_2 \cdot 2H_2O$, 89.4 mM K_2HPO_4, 56.4 mM $NaH_2PO_4 \cdot H_2O$, 8.6 mM NaCl and trace metals as 1.9 µM H_3BO_3, 0.86 µM $CuSO_4 \cdot 5H_2O$, 7.7 µM $ZnSO_4 \cdot 7H_2O$, 0.75 µM $MnSO_4 \cdot H_2O$, 0.26 µM $NiCl_2 \cdot 6H_2O$, 0.31 µM $Na_2MoO_4 \cdot 2H_2O$. The total carbon-equivalent substrate concentration of 100 mM C was added as 50 mM C glucose and 50 mM C sodium benzoate. No exogenous supply of Fe was provided. However, the background dissolved Fe content was determined to be 650 nM by inductively coupled plasma atomic emission spectroscopy (ICP-AES, Spectro Analytical). In order to ensure nutrient limitation, 0.09 mM of a strong metal chelator disodium-EDTA was added following the addition of the organic substrates. The concentration of EDTA to be added, was determined by ensuring that bioavailable equilibrium Fe concentration was within the nutrient limited range, and was obtained using Visual MINTEQ (version 3.1) (Vasil et al., 1999; Kim et al., 2009).

Hence, the two conditions of nutrient limitation obtained were without (Fe-limited) or with (Fe-starved) EDTA.

For the growth experiments with each Fe condition, the cells (three biological replicates) were transferred twice in the growth medium (containing major and minor salts, carbon source, without or with EDTA) to ensure the cells were acclimated. Biomass growth was monitored by measuring the optical density at 600 nm (OD_{600}) using an Agilent Cary UV-visible spectrophotometer (Santa Clara, California). An exponential growth rate (h^{-1}) was determined via regression analysis. Measurement of cell dry weight in grams (g_{CDW}) as a function of exponential OD_{600} was obtained following lyophilization of sample aliquots (1.5-mL) using a Labconco (Kansas City, MO, USA) Freeze-Dryer System. A conversion factor of 0.586±0.2 $g_{CDW}\,L^{-1}$ per OD_{600} and 0.6±0.2 $g_{CDW}\,L^{-1}$ per OD_{600} was determined for the Fe-limited and Fe-starved cells, respectively.

2.2 Substrate Consumption and intracellular metabolite labeling

To quantify the rate of consumption of substrate, 0.5-mL of samples (three biological replicates) were harvested during the exponential growth of the cells and filter-centrifuged (Sigma Aldrich Spin-X 0.22 µm filters) at 9391*g* for 5 mins at 4°C (Centrifuge 5423 R, Eppendorf, Hauppauge, NY). The supernatants were stored at 4°C until analysis for simultaneous quantification of glucose and benzoate by ^{1}H nuclear magnetic resonance (NMR). In preparation for analysis, 200-µL of filtered sample was mixed with 60-µL of 100% D_2O, 50-µL of 6 mM 2,2-dimethyl-2-silapentane-5-sulfonate (DSS) as an internal standard, 240-µL of 100 mM sodium bicarbonate as a pH control and 50-µL of 10 mM sodium-azide as an antimicrobial agent (Kukurugya, 2017). The ^{1}H NMR measurements were performed using a Varian Unity INOVA 600-MHz NMR

spectrometer at 25°C with a relaxation delay of 5s, recording of 16 scans per sample and a receiver gain of 32 dB. The consumption rates (mmol g_{CDW}^{-1} h^{-1}) of glucose and benzoate by the exponentially-growing cells were determined via regression analysis.

Intracellular incorporation of assimilated substrates was monitored by determining metabolite labeling patterns following growth on two different labeling schemes. [U-$^{13}C_6$]-glucose and unlabeled benzoate; [1,5,6-$^{13}C_6$]-glucose and unlabeled benzoate (labeled substrates were purchased from Cambridge Isotopes (Tewskbury, MA, USA) or Omicron Biochemicals (South Bend, IN, USA)) cultures (three biological replicates) were grown twice in minimal media containing the labeled substrate combination specified above. The isotopic labelling patterns were retrieved using the Metabolomics Analysis and Visualization Engine (MAVEN) software package (Clasquin et al., 2012) and the ^{13}C-labelled fractions were corrected for natural ^{13}C abundance. To determine that the cells were at metabolic pseudo-steady state, both labeling patterns and the metabolite levels were determined at two time points during exponential phase.

2.3 Extracellular Metabolite Excretion

For quantitation of extracellular metabolic excretion, samples (three biological replicates) were harvested at several time points throughout the exponential growth phase and 50-µL of filtered supernatant was diluted 1:10 or 1:100 with LC-MS grade water (Fisher Scientific, Pittsburgh, PA) before analysis via LC-MS (*see section 4*). The excretion rates (µmol g_{CDW}^{-1} h^{-1}) for metabolites of interest (gluconate, a-KG, succinate, pyruvate, citrate, oxaloacetate, glutamate, fructose 6-phosphate, glucose 6-phosphate, malate, dihydroxyacetone phosphate, phosphoenolpyruvate) were computed via regression analysis.

2.4 Metabolomics Analysis via LC-MS

Samples were analyzed by reversed-phase ion-pairing LC via ultra-high performance LC (UHPLC; Thermo Scientific DionexUltiMate 3000) coupled to high-resolution accurate-mass mass spectrometer (MS; Thermo Scientific Q Exactive) with electrospray ionization operated in full-scan negative mode (m/z range 70-900). Mobile phases for the LC-MS consisted of solvents A and B: Solvent A was composed of 97:3 (v/v) LC-MS grade H_2O:methanol with 15 mM acetic acid and 10 mM tributylamine; Solvent B was pure methanol. The flow rate was 180 µL min^{-1} for the duration of a single sample run (25 min). The solvent gradient with respect to solvent A was: 0 min, 100%; 2.5 min, 100%; 5 min, 80%; 7.5 min, 80%; 10 min, 45%; 12 min, 45%; 14 min, 5%; 17 min, 5%; 18 min, 0%; 25 min, 0% (Kukurugya, 2017). An injection sample of 10-µL was used and the column (Acquity UPLC Water 1.7µm particle size) temperature was set to 25°C (Kukurugya, 2017; Sasnow et al, 2016). The metabolites of interest were gluconate, 2-keto gluconate, glucose-6-phosphate, fructose-6-phosphate, fructose-1,6-bisphosphate, dihydroxyacetone phosphate, Glyceraldehyde-3-phosphate, 3-phosphoglycerate, phosphoenolpyruvate, pyruvate, citrate, α-ketoglutarate, succinate, fumarate, malate, acetyl coenzyme-A, sedoheptulose-7-phosphate, ribose-5-phosphate, ribulose-5-phosphate, erythrose-4-phosphate, glutamine and aspartate. Aspartate was taken as a surrogate for oxaloacetate (OAA) owing to the direct synthesis of aspartate from OAA (Kukurugya, 2017; Sasnow et al. 2016; Amador-Noguez et al. 2010).

2.5 Pyoverdine Quantitation

The extracellular amount of secreted PVD siderophore was determined in pH-adjusted (pH 7) bacterial supernatants (three biological replicates) as done previously using absorbance (400 nm)

(Ferret et al. 2014; Sasnow et al. 2016). A PVD standard (Sigma Aldrich) isolated from a *P. flourescens* strain was used for quantitation. It was verified via LC-MS that both the standard and the PVD secreted by the strain under study (KT2440) possessed the same dihydroxyquinoline-type chromophore (Wei and Aristilde, 2015). The PVD excretion rate (μmol g_{CDW}^{-1} h^{-1}) of the exponentially-growing liquid cultures was calculated via regression analysis.

2.6 Metabolic Flux Analysis

The software suite 13CFLUX2 package (http://www.13cflux.net) was used to perform a metabolic flux analysis (MFA) for quantitative modelling of fluxes through central carbon metabolism, and biosynthetic fluxes for biomass growth and PVD biosynthesis. The MFA was constrained using the following experimental data (averaged values ± standard deviation): substrate uptake rate, metabolite excretion rates, PVD secretion rate, labeling patterns of metabolites from the long-term labeling experiments with [1,5,6-$^{13}C_3$]-glucose and unlabeled benzoate, and calculated effluxes toward biomass production. Substrate consumption rates and metabolite excretion rates were measured using NMR analysis and LC-MS analysis, respectively, as described above. Using the biomass growth rates determined experimentally (as described above) and published biomass composition of *P. putida* KT2440 (Van Durren et al., 2013), the effluxes towards biomass production from glycolytic, PP and TCA cycle metabolites were calculated (Nikel et al., 2015; Sasnow et al., 2016; Kukurugya, 2017). The software was applied to set up the modeled metabolic network of reactions. Initial flux values at the start of the optimization procedure were set based on published values (Nikel et al., 2015; Sasnow et al., 2016; Kukurugya, 2017). The model-estimated labeling patterns from the modeling of the stoichiometric reaction network were optimized on the measured labeling pattern.

3. RESULTS AND DISCUSSION

3.1 Growth phenotype and substrate consumption

We determined the exponential growth rates and the carbon uptake rate in *P. putida* KT 2440 cells grown on 100 mM C of 1:1 glucose:benzoate mixture under both Fe-limited and Fe-starved conditions. A previous study of Fe-replete *P. putida* KT2440 grown on the same carbon-equivalent glucose:benzoate mixture reported a growth rate of $0.93\pm0.1 h^{-1}$ (Kukurugya, 2017). Remarkably, the growth rate obtained for Fe-limited and Fe-starved cells was found to be in close agreement with the Fe-replete cells, at $0.89\pm0.18 h^{-1}$ and $0.89\pm0.11\ h^{-1}$, respectively (Fig 3). This similarity in growth rates implied a coping mechanism of the *P. putida* cells in response to Fe-limitation towards maintenance of biomass growth from the mixed-substrate growth medium. By contrast, for *P. putida* KT2440 cells grown solely on glucose alone, there was a seven-fold reduction in growth rate, from $0.60\pm0.04\ h^{-1}$ for Fe-replete cells to $0.08\pm0.02\ h^{-1}$ in Fe-limited cells (Sasnow et al., 2016). We note here that mixed substrate-grown cells under Fe-starvation exhibited a clear diauxic growth wherein the second growth phase ($0.26\pm0.08\ h^{-1}$) was a four-fold less than the growth rate of $0.89\pm0.11\ h^{-1}$ recorded for the first phase (Fig 2 and Fig 3).

To evaluate the influence of substrate consumption on the growth phenotypes, we obtained the extracellular depletion of glucose and benzoate (Fig 4). For Fe-replete cells grown on the mixed substrate, the carbon-equivalent consumption rate of glucose and benzoate was reported to be 19.8 ± 4.4 mmol C $g_{CDW}^{-1}\ h^{-1}$ and 27.2 ± 8.1 mmol C $g_{CDW}^{-1}\ h^{-1}$, respectively (Kukurugya, 2017). Therefore, the total Fe-replete carbon consumption rate of the substrate mixture was 47.0 ± 11.1 mmol C $gCDW^{-1}\ h^{-1}$. Under Fe-limitation, we obtained a total consumption rate of 70.1 ± 17.18 mmol C $gCDW^{-1}\ h^{-1}$ (Fig 4). In accordance with the aforementioned diauxic growth of the Fe-starved cells, the trend of the carbon consumption was divided across two phases. In

the first phase, the benzoate consumption rate was measured to be 52.2±11.4 mmol C g_{CDW}^{-1} h^{-1} but the glucose consumption rate was minimal at 2.0±0.9 mmol C g_{CDW}^{-1} h^{-1} (Fig 4). In the second phase, the glucose consumption, which began upon near-complete benzoate depletion, was determined to be 23.8±7.0 mmol C g_{CDW}^{-1} h^{-1} (Fig 4).

Therefore, these data indicated that the benzoate consumption rate was greater than the glucose consumption rate by, on average, 57.2% in Fe-limited cells and, during the first growth phase, by 96% in Fe-starved cells (Fig 4) whereas an equal rate of benzoate and glucose consumption was reported for Fe-replete cells. Thus, these findings implied increased preference towards an aromatic substance as a function of decreased Fe availability. In order to confirm the preferential substrate consumption and to understand Fe-dependent carbon metabolism of mixed substrate, we investigated the investment of assimilated glucose and benzoate into the intracellular metabolites into the different central metabolic pathways: the ED pathway, reverse EMP pathway, PP pathway and the TCA cycle.

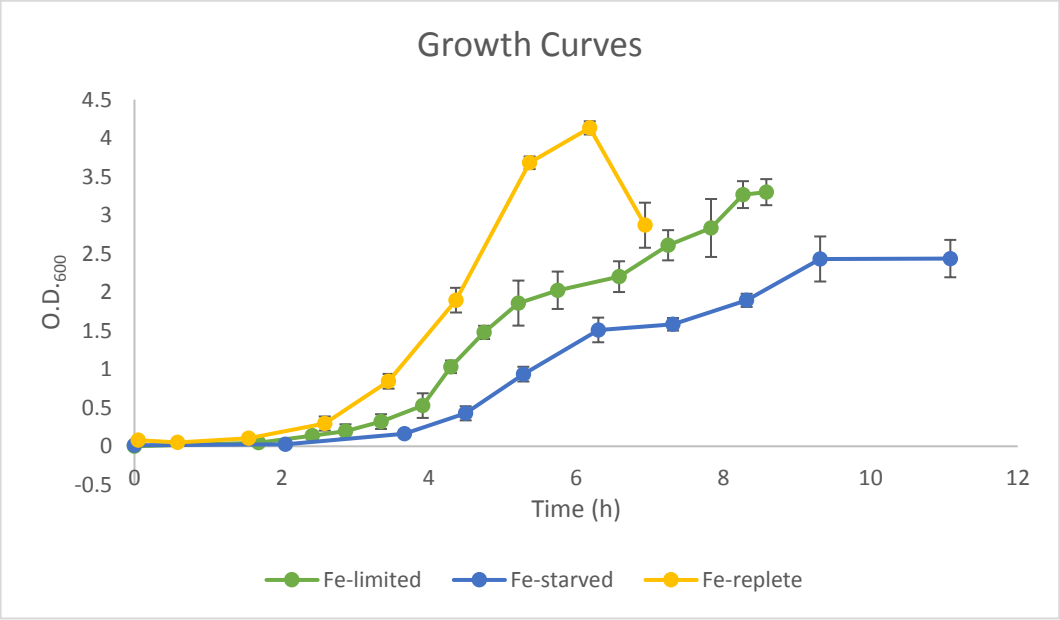

Fig 2: Growth curves for *P. putida* KT2440 cells grown on Fe-replete (Kukurugya, 2017), Fe-limited and Fe-starved glucose-benzoate mixture.

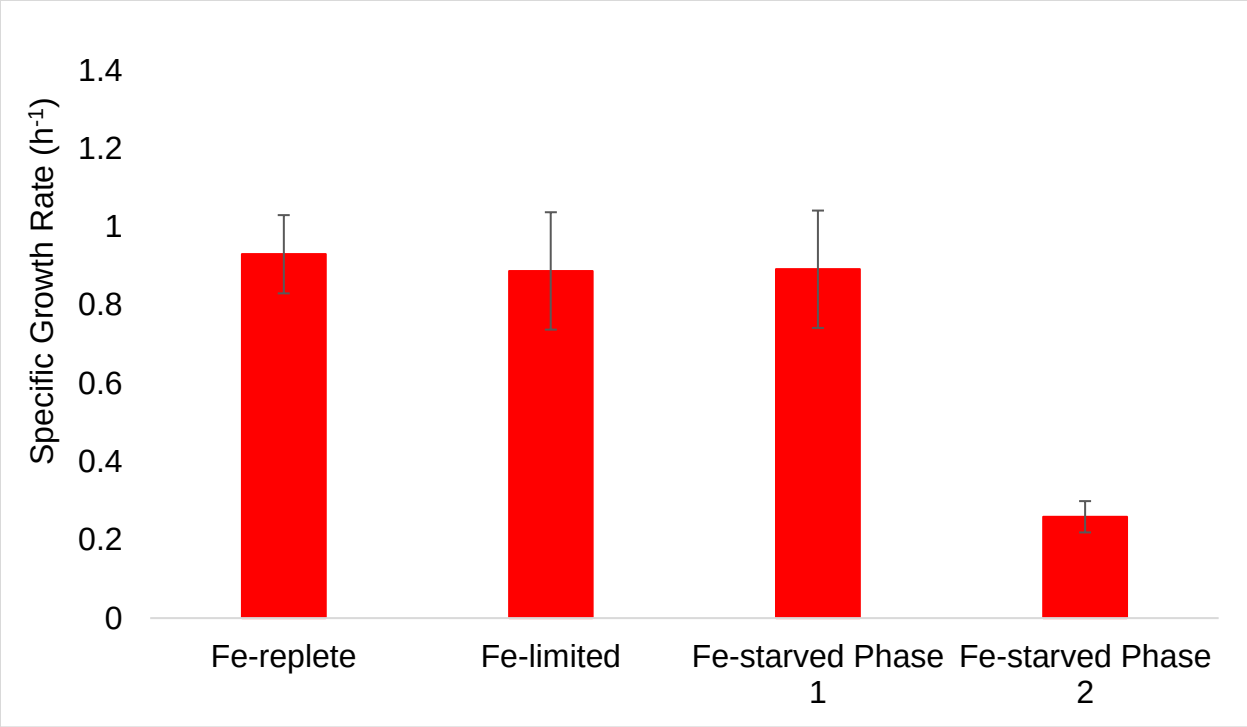

Fig 3: Growth rates (h^{-1}) for *P. putida* KT2440 cells grown on glucose-benzoate mixture during Fe-replete (Kukurugya, 2017), Fe-limited and Fe-starved conditions.

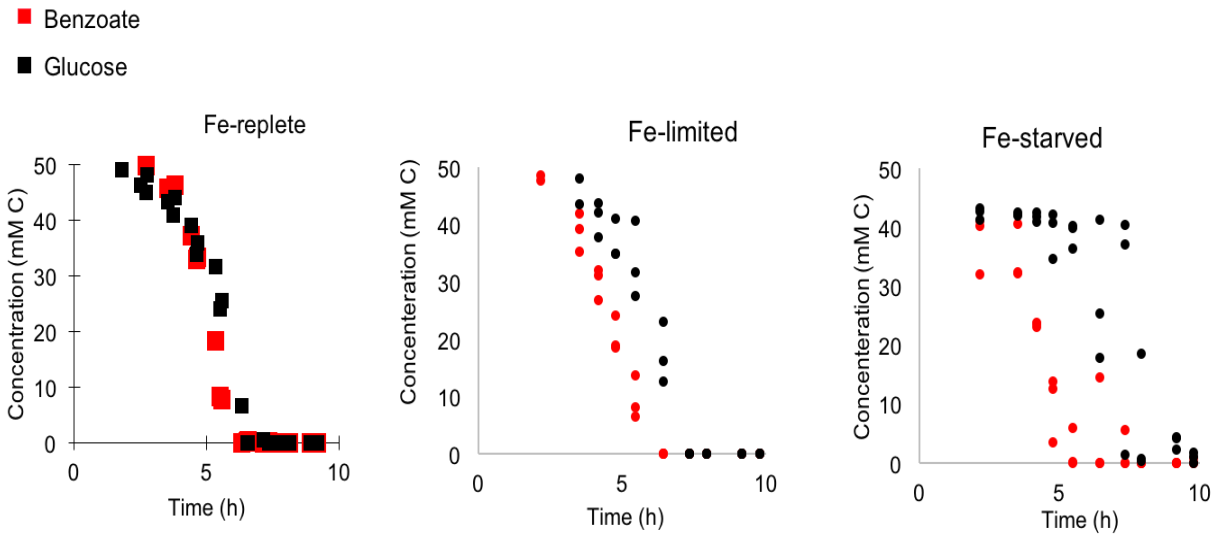

Fig 4: Consumption of glucose and benzoate for *P. putida* KT2440 cells grown on Fe-replete (Kukurugya, 2017), Fe-limited and Fe-starved glucose-benzoate mixture.

Fig 5: Carbon equivalent consumption rates (mmol C $gCDW^{-1}$ h^{-1}) for *P. putida* KT2440 cells grown on Fe-replete (Kukurugya, 2017), Fe-limited and Fe-starved glucose-benzoate mixture.

3.2 Fe-dependent substrate incorporation

The metabolic network model for the metabolism of glucose and benzoate in Fe-replete cells was previously elucidated using ^{13}C tracer experiments by Kukurugya (2017). In order to understand Fe-dependent substrate incorporation, we first monitored the metabolite labelling in Fe-limited and Fe-starved *P. putida* KT2440 cells grown on fully-labelled [U-$^{13}C_6$]-glucose with unlabeled benzoate (Fig. 6, Fig. 7, Fig. 8, Fig. 9). To examine that the *P. putida* KT2440 cells attained pseudo-steady state, we obtained long-term isotopic enrichment of its intracellular metabolites at two different times (OD_{600} of 0.4 and 0.8) (Fig. S3, Fig. S4, and Fig. S5). The data obtained under the Fe-replete conditions for the same labeling schemes revealed that the cells partitioned carbons derived from benzoate to the TCA cycle and carbons derived from glucose to the ED pathway, reverse EMP pathway and the PP pathway (Kukurugya, 2017). We compared these results with those obtained with cells grown here with cells grown Fe-limited and Fe-

starved conditions (Fig. 8, Fig. 9, and Fig. 10). First, we monitored the labeling patterns of metabolites into the ED and reverse EMP pathways (Fig. 6 and Fig. 7). In accordance with uptake and initial catabolism of the labeled glucose, we found that Glucn and 6PG was almost completely fully ^{13}C-labeled (99.9 ± 0.4%, 95.5 ± 1.2% and 99.9 ± 0.0% for Fe-replete, Fe-limited and Fe-starved cells, respectively) (Fig 7). As the keto-pathway is absent in *Pseudomonas putida* KT2440, benzoate-derived carbons can enter the TCA cycle through succinate and acetyl-coA, via the ortho-pathway (Fig. 8). Through the established flow of the TCA cycle, carbons from succinate can be routed to malate and OAA and be subsequently introduced to the EMP pathway via the malate shunt to pyruvate and two anaplerotic reactions, OAA to pyruvate and OAA to PEP (Fig. 8). Pyruvate can in turn be converted to acetyl co-A directly upstream of the TCA cycle. In the direction of gluconeogenesis, pyruvate may be converted to 3PG, which can then be converted to GAP and DHAP (Fig. 6). The appreciable triply ^{13}C-labeled fraction of FBP (18.9 ± 0.6% and 17.3 ± 1.1 %, correspondingly for Fe-limited and Fe-starved cells), F6P (24.2 ± 2.7 % and 25.4 ± 4.9 % for Fe-limited and Fe-starved conditions, respectively) and G6P (9.6 ± 1.3% and 10.1 ± 0.8%), indicated a small gluconeogenic flux of benzoate-derived carbons in the upper portion of the reverse EMP (Fig. 7). This increase in the triply ^{13}C-labeled fraction, which was consistent with enhanced contribution of benzoate carbons towards the ED and reverse EMP pathways. However, DHAP had a greater fraction of non-labeled carbons: 6.7 ± 0.1%, 31.7 ± 0.4% and 32.2 ± 0.2% in Fe-replete, Fe-limited and Fe-starved cells, respectively (Fig. 7). Thus, the DHAP labeling also indicated that incorporation of benzoate-derived carbons through gluconeogenic flux was greater in the Fe-limited and Fe-starved cells than in Fe-replete cells. With regards to the PP pathway, the presence of doubly and triply ^{13}C labeled R5P and X5P indicated that carbon from benzoate was

present (Fig. 10). In addition, absence of non-labeled carbon in 6-PG across all Fe-conditions confirmed that the non-labeled carbon was introduced to the PP pathway through non-oxidative branch, i.e., via GAP and F6P.

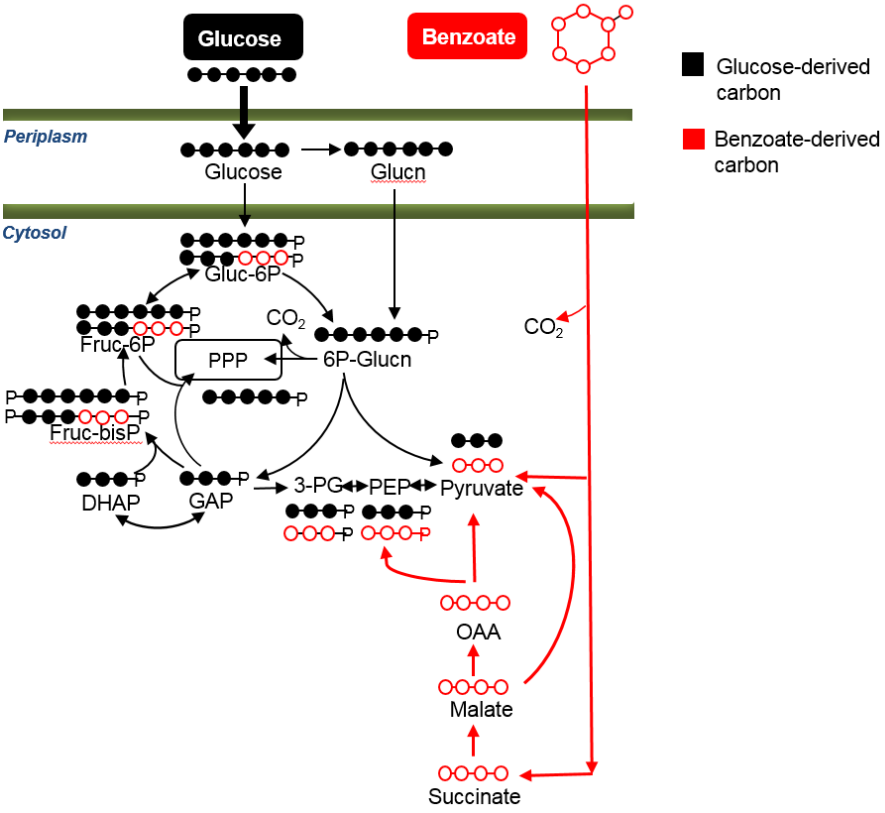

Fig 6: Schematic representation of ^{13}C-labeled metabolites in ED and reverse EMP when grown on [U-$^{13}C_6$]-glucose and unlabeled benzoate (Kukurugya, 2017). Metabolite abbreviations are the same as in Fig 1.

Fig 7: Labeling of the ED and reverse EMP pathway metabolites in pseudo-steady state at optical density (OD_{600}) 0.4 in Fe-limited and Fe-starved cells; 0.5 in Fe-replete cells (Kukurugya, 2017) when grown on [U-$^{13}C_6$]-glucose and unlabeled benzoate. Metabolite abbreviations are the same as in Fig 1.

The ^{13}C-labeling pattern of metabolites in the TCA cycle were in accordance with the canonical routing of carbon through the pathways mentioned above (Fig. 8). Acetyl-CoA can be either non-labeled or doubly ^{13}C-labeled, owing to the decarboxylation of unlabeled or triply ^{13}C-labeled pyruvate, respectively. Non-labelled acetyl-coA can also be generated from carbon entry through the ortho-pathway of benzoate breakdown. Aspartate was taken as surrogate to OAA, and it was observed that in the Fe-replete conditions, OAA was almost 59.3±0.1% non-labeled (Kukurugya, 2017). However, in the Fe-stressed conditions the non-labeled fractions increased with the extent of Fe-limitation accordingly. In the Fe-limited cells, OAA was 91.2±0.4% non-labeled while in the Fe-starved condition, it was 95.8±0.4% non-labeled (Fig 9), therefore, confirming our hypothesis of an increase in aromatic substrate incorporation, with the increase in the extent of Fe-limitation. This trend was consistent among all the metabolites in the TCA cycle, namely, succinate, malate, fumarate, pyruvate, a-kg and PEP, suggesting the incorporation of carbon from the unlabeled aromatic substrate. Citrate was majorly non-labeled due to the combination of mostly non-labeled acetyl-coA with mostly non-labelled OAA. Fully labeled fractions of acetyl-coA and glyoxylate combine to yield 27.6±0.8% and 27.8±1.0% fully labeled malate in the Fe-limited and Fe-starved conditions, respectively.

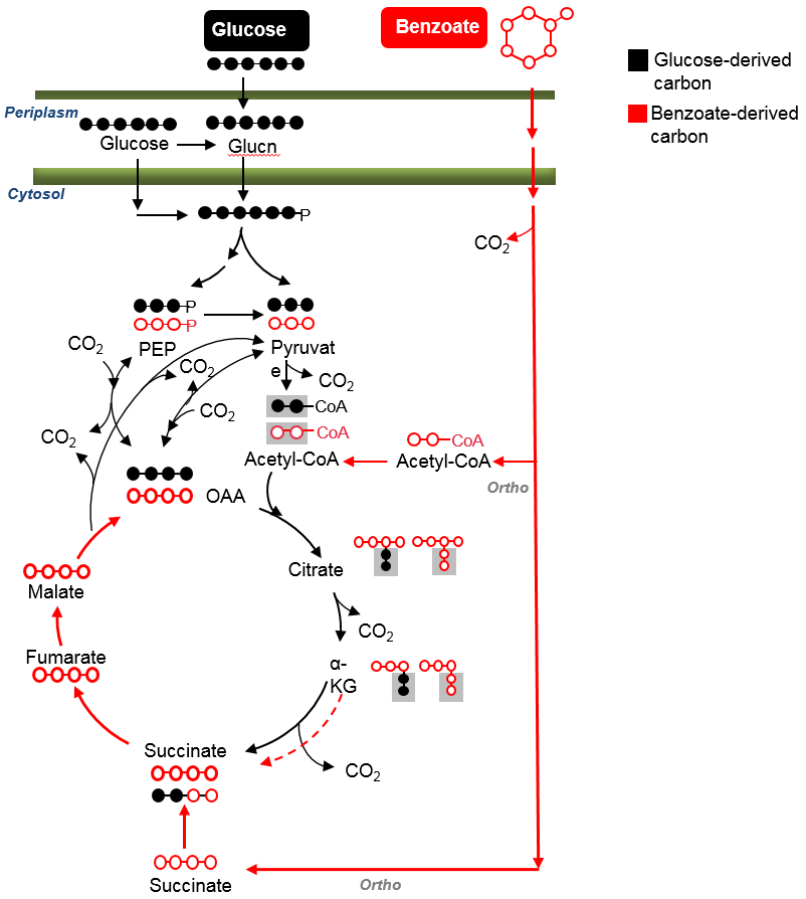

Fig.8: Schematic representation of ^{13}C-labeled metabolites in central carbon metabolism when grown on [U-$^{13}C_6$]-glucose and unlabeled benzoate in reverse EMP pathway and TCA cycle (Kukurugya, 2017).

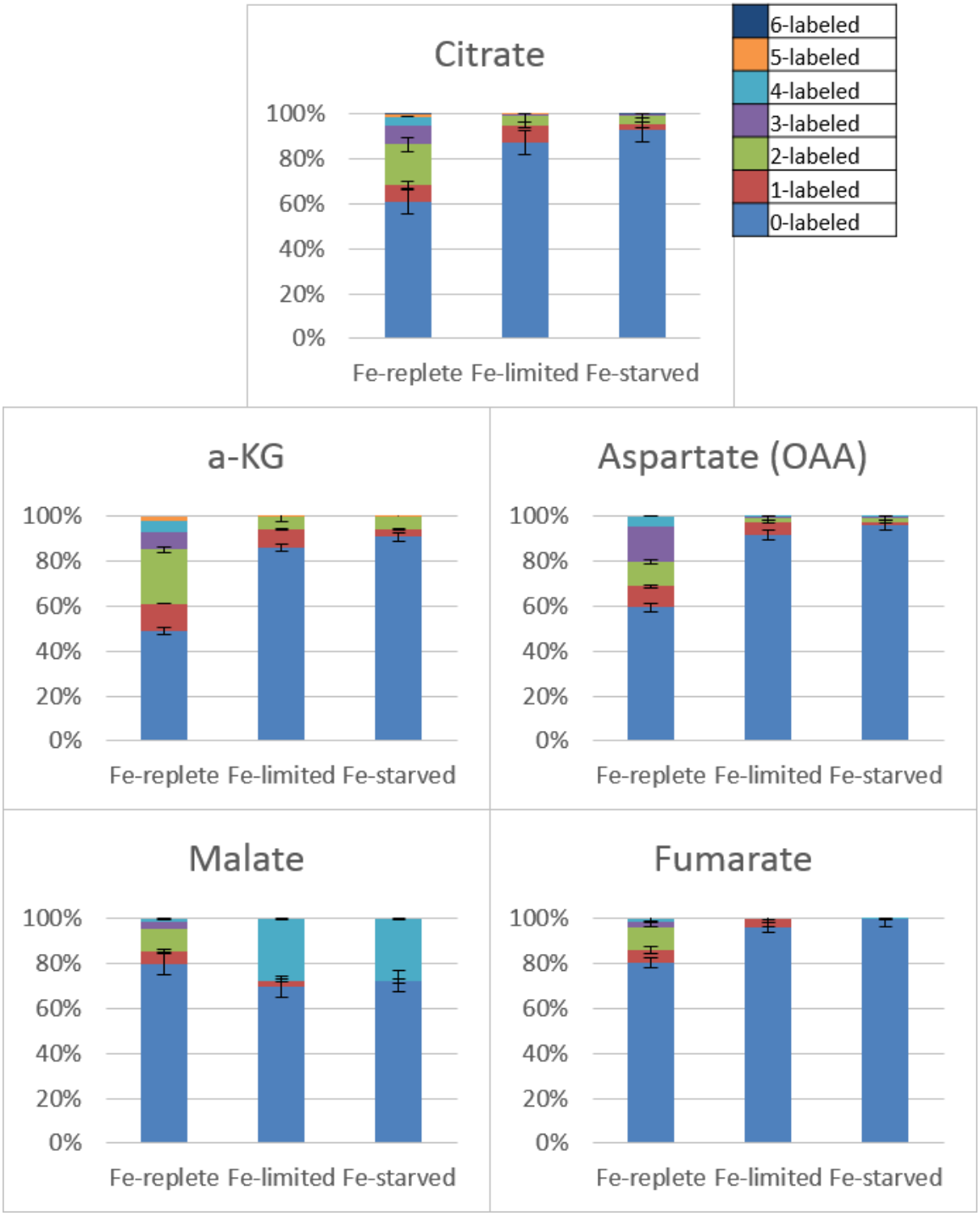

Fig 9: Labeling of the TCA cycle metabolites in pseudo-steady state at optical density (OD_{600}) 0.4 in Fe-limited and Fe-starved cells; 0.5 Fe-replete cells (Kukurugya, 2017) when grown on [U-$^{13}C_6$]-glucose and unlabeled benzoate. Metabolite abbreviations are the same as in Fig 1.

Fig 10: Labeling of the PP pathway metabolites in pseudo-steady state at optical density (OD_{600}) 0.4 in Fe-limited and Fe-starved cells; 0.5 Fe-replete cells (Kukurugya, 2017) when grown on [U-$^{13}C_6$]-glucose and unlabeled benzoate. Metabolite abbreviations are the same as in Fig 1.

In summary, glucose-derived carbons mainly populated the ED and reverse EMP pathways across all conditions, with a minor contribution of benzoate-derived carbons in G6P, DHAP, FBP and F6P for the Fe-limited and Fe-starved conditions. The TCA cycle was mainly dominated by benzoate-derived carbons with a minimal input of glucose-derived carbon. Citrate, a-KG, PEP, fumarate and OAA displayed a 30-35% increase in the non-labeled fraction of carbon in the Fe-stressed conditions in comparison with the Fe-replete conditions. Further analysis into the selective partitioning of the metabolite labelling, as required for the metabolic flux analysis (MFA) was obtained by performing additional long-term isotopic enrichment of intracellular metabolites on [1,5,6-$^{13}C_3$]-glucose and unlabeled benzoate.

3.3 Metabolic Network Structure

We elucidated the selective partitioning of both glucose and benzoate-derived carbons in specific pathways in the metabolic network. We performed long-term isotopic enrichment of intracellular metabolites by growing cells on [1,5,6-$^{13}C_3$]-glucose and unlabeled benzoate under Fe-limited and Fe-starved conditions. To ascertain that the isotopic enrichment was at steady-state, we compared the ^{13}C-labeling patterns of metabolites extracted from cells at two different times (OD_{600} of 0.4 and 0.8) during the exponential growth phase (Fig. 12, 13, 14, 16, 17, 18, 20, 21 and 22). These results were similar to the metabolic network structure elucidated for Fe-replete *P. putida* cells grown on a mixed substrate of glucose and benzoate (Kukurugya, 2017).

We began by establishing the network of carbon flow for initial glucose catabolism, the ED pathway and the reverse EMP pathway (Fig. 11). We found that the oxidation of triply ^{13}C-labeled glucose yielded nearly completely triply ^{13}C-labeled gluconate in the periplasm of Fe-limited (93.9±6.8%) cells and in the first (98.9±0.2%) and second (99.9±0.1%) growth phases of Fe-starved cells (Fig. 12, Fig 13, Fig. 14). Accordingly, the phosphorylated metabolites in glucose catabolism, G6P and 6-PG, were also predominantly triply ^{13}C-labeled, 53.8±8.0% and 86.4±4.1%, respectively in the Fe-limited growth medium; 63.3±4.2% and 76.4±2.1%, respectively in the first phase of Fe-starved growth and finally, 62.3±1.0 and 78.9±0.1, respectively in the second phase of Fe-starved growth (Fig. 12, Fig. 13, Fig. 14). The precursors of 6-PG are both gluconate and G6P and therefore, the higher enrichment in triply ^{13}C-labeled 6-PG compared to G6P inferred greater flux of gluconate towards the biosynthesis of 6-PG (Fig. 12, Fig. 13 and Fig. 14). Moving further down the ED pathway, triply ^{13}C-labeled 6-PG splits into singly ^{13}C-labeled pyruvate (38.7±4.0%, 11.6±2% and 36.7±4% in Fe-limited, Phase 1 Fe-starved and Phase 2 Fe-starved cells, respectively) and doubly ^{13}C-labeled GAP (91.7±0.0%,

64.6±4.6% and 94.9±4% in Fe-limited, Phase 1 Fe-starved and Phase 2 Fe-starved cells, respectively) (Fig. 12, Fig. 13, and Fig. 14). DHAP, an isomer of GAP exhibited the similar labeling trend (Fig. 12, 13 and 14). The presence of doubly ^{13}C-labeled pyruvate under the Fe-limitation (42.4±4%), and Fe-starvation (4.4±0.1% for phase 1 and 23.7±4.3% for phase 2) underlined the contribution of both the ED pathway and the metabolites downstream of GAP to form pyruvate (Fig. 12, 13 and 14). Doubly ^{13}C-labeled forms of 3-PG and PEP were, respectively 45.8±6.3% and 33.7±3.6% in Fe-limited cells and 21.7±5.0% and 8.7±1.0% in phase 1 of Fe-starved cells (Fig. 12 and Fig. 13). However, during the second phase of growth, there was a significant increase in the doubly labeled fractions of 3-PG and PEP (91.5±5% and 86.1±0.0%, respectively) (Fig. 14), thereby implying a greater incorporation of glucose-derived carbons. The decrease in the non-labeled fraction of pyruvate (39.4±0.8%) was accompanied by an increase in the doubly ^{13}C-labeled fraction (23.7±4.3%) (Fig. 14). Therefore, the data confirmed that non-labeled benzoate-derived carbons were incorporated into 3-PG, PEP and pyruvate under Fe-limitation and during the first growth phase under Fe-starvation whereas glucose-derived carbons were primarily populated by 3-PG, PEP and pyruvate in the second growth phase of Fe-starved cells.

The fraction of non-labeled DHAP was significantly low in the second phase of Fe-starved growth (3.8±2.0%) and in the Fe-limited (8.5±0.0%) condition. However, during the growth on the first phase of Fe-starvation, non-labeled DHAP was 35.2±5.0%, indicating significant assimilation of benzoate-derived carbons even upstream of 3-PG. In agreement with the metabolic framework developed for the Fe-replete cells (Kukurugya, 2017), we found that through the reverse EMP pathway, the ED pathway-generated doubly ^{13}C-labeled GAP combines

with its isomer DHAP to form quadruply ^{13}C-labeled FBP, which then dephosphorylates to F6P (Fig.11).

Proceeding further down the reverse EMP pathway, we obtained quadruply ^{13}C-labeled forms of both FBP and F6P during growth on Fe-limited medium (respectively, 63.4 ± 5.5% and 63.1 ± 3.0%), phase 1 (respectively, 36.2± 7.0% and 20.8 ± 4.0%) and phase 2 (respectively, 81.3±6.9% and 47.4±3.7%) of the Fe starved condition (Fig. 12, 13 and 14). The formation of G6P can result either from the isomerization of F6P or from the phosphorylation of glucose wherein the first reaction would generate quadruply ^{13}C-labeled G6P and the second reaction would provide only triply ^{13}C-labeled G6P (Fig. 11). We found that quadruply ^{13}C-labeled fraction of G6P in cells grown under Fe-limitation (39.5.4±8.5%) and in the second phase of Fe-starvation (24.2±0.1%) was higher than quadruply ^{13}C-labeled fraction of G6P in the first phase of Fe-starved cells (10.1±2.9%). This implied a reduced recycling flux of assimilated glucose through the first growth phase of Fe-starved cells.

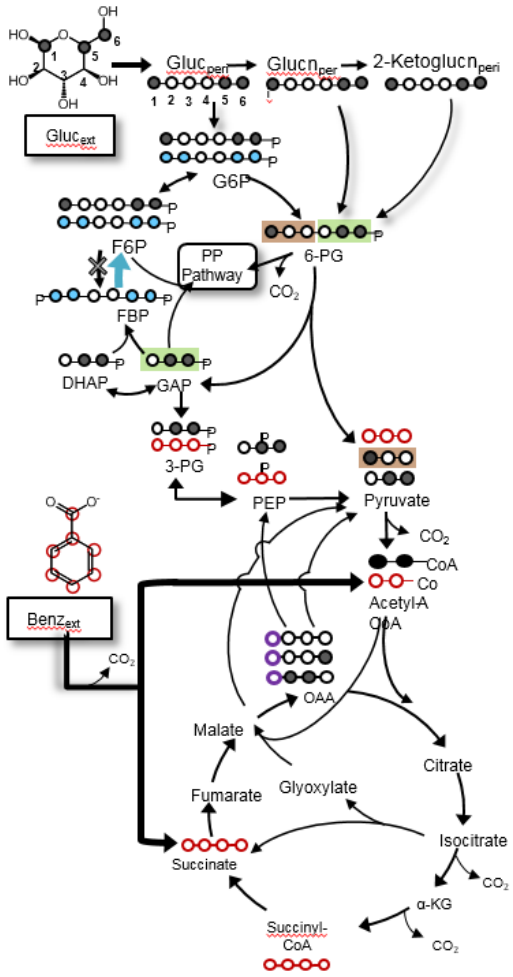

Fig. 11: Schematic representation of ^{13}C-labeled metabolites in central carbon metabolism when grown on [1,5,6-$^{13}C_3$]-glucose and unlabeled benzoate in ED and reverse EMP pathways. Metabolite abbreviations are the same as in Fig 1 (Figure courtesy of Dr. Ludmilla Aristilde, 2017).

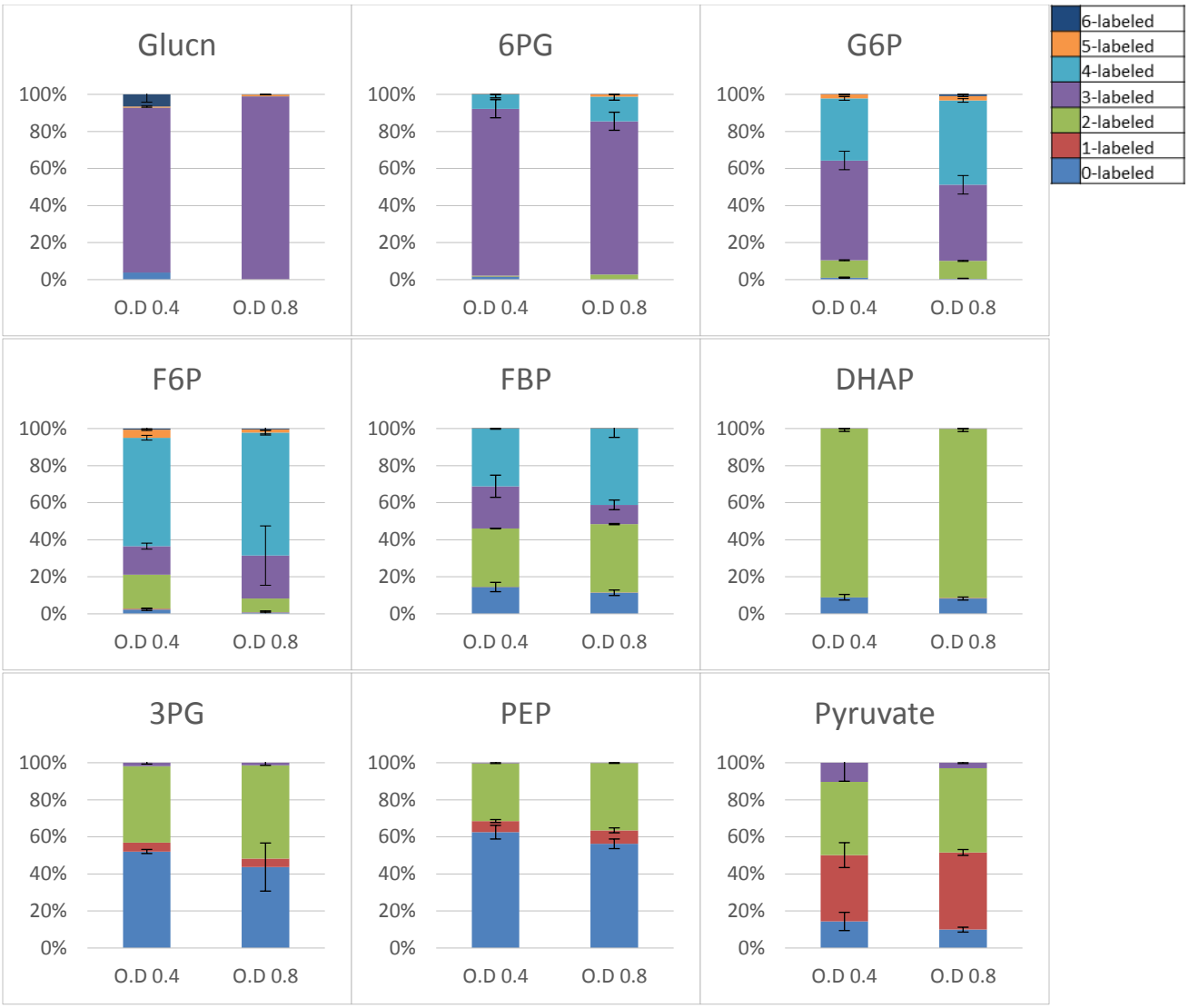

Fig. 12: The isotopic labeling fractions, with standard deviations, for intracellular metabolites in the ED and EMP pathways when grown on [1,5,6-$^{13}C_3$]-glucose and unlabeled benzoate under Fe-limitation at $O.D_{600}$ 0.4 and 0.8. Metabolite abbreviations are the same as in Fig 1.

Fig. 13: The isotopic labeling fractions, with standard deviations, for intracellular metabolites in the ED and EMP pathways when grown on [1,5,6-$^{13}C_3$]-glucose and unlabeled benzoate during the first phase of growth under Fe-starvation at $O.D_{600}$ 0.4 and 0.8. Metabolite abbreviations are the same as in Fig 1.

Fig. 14: The isotopic labeling fractions, with standard deviations, for intracellular metabolites in the ED and EMP pathways when grown on [1,5,6-$^{13}C_3$]-glucose and unlabeled benzoate during second phase of growth under Fe-starvation at $O.D_{600}$ 0.4 and 0.8. Metabolite abbreviations are the same as in Fig 1.

Pertaining to the PP pathway, the labeling patterns of Xu5P and R5P indicated the participation of both the oxidative and non-oxidative routes of the PP pathway as reported in Fe-replete cells (Fig. 15). Through the oxidative pathway, a decarboxylation reaction generates doubly ^{13}C-labeled pentose-phosphate metabolites from triply ^{13}C-labeled 6-PG (Fig. 15). During growth on the Fe-limited condition, we measured the doubly ^{13}C-labeled forms of R5P and Xu5P at, correspondingly, 42.0 ± 0.0% and 38.2±5.4%; the corresponding values during growth on the

Fe-starvation were 55.7 ± 0.2% and 55.8± 0.3%, respectively for the first phase, and 65.6±6.2% and 63.5±3.7% for the second phase (Fig. 16, 17 and 18). Given the high fraction of 6-PG in triply ^{13}C-labeled forms, the relatively low fraction of doubly ^{13}C-labeled R5P and Xu5P indicated that the oxidative PP pathway was not the major biosynthetic route for these PP metabolites under both growth conditions, as previously reported for *P. putida* KT2440 cells (Sasnow et al., 2016; Kukurugya, 2017). Through the non-oxidative pathway, the labeling patterns of F6P and GAP mentioned above combine through a series of reactions to generate eventually quadruply ^{13}C-labeled Xu5P and R5P. However, the ^{13}C-labeling pattern of S7P, another intermediate in the PP pathway, indicated an alternate routing of carbons within the non-oxidative PP pathway for each condition (Fig. 15). There are two ways of generating S7P: (1) via the transketolase reaction wherein the first two carbons from Xu5P combines with R5P and (2) via the transaldolase reaction where the first three carbons from F6P combines with E4P. The transketolase reaction would therefore primarily yield quadruply and sextuply ^{13}C-labeled forms of S7P whereas the transaldolase reaction would yield mostly quadruply ^{13}C-labeled S7P and some quintuply ^{13}C-labeled S7P (as the backward flux of the transaldolase reaction would produce triply ^{13}C-labeled E4P that would yield the quintuply ^{13}C-labeled S7P when combined with F6P in the forward flux (Fig. 15). When fed on the Fe-starved medium, the cells generated two main labeled forms of S7P: primarily quadruply ^{13}C-labeled (26.5±6.9% and 40.0±1.8% for the first and second phase, respectively) and doubly ^{13}C-labeled (36.2±1.8% and 28.6±0.4% for the first and second phase, correspondingly) (Fig. 17 and 18). On the other hand, the cells fed on the Fe-limited mixture had primarily quadruply ^{13}C-labeled S7P (49.1 ± 3.5%) and sextuply ^{13}C-labeled S7P (17.4 ± 1.5%) (Fig. 16). Therefore, S7P was primarily made from the transaldolase

reaction during Fe-starved growth but primarily from the transketolase reaction downstream of the oxidative PP pathway during Fe-limited growth.

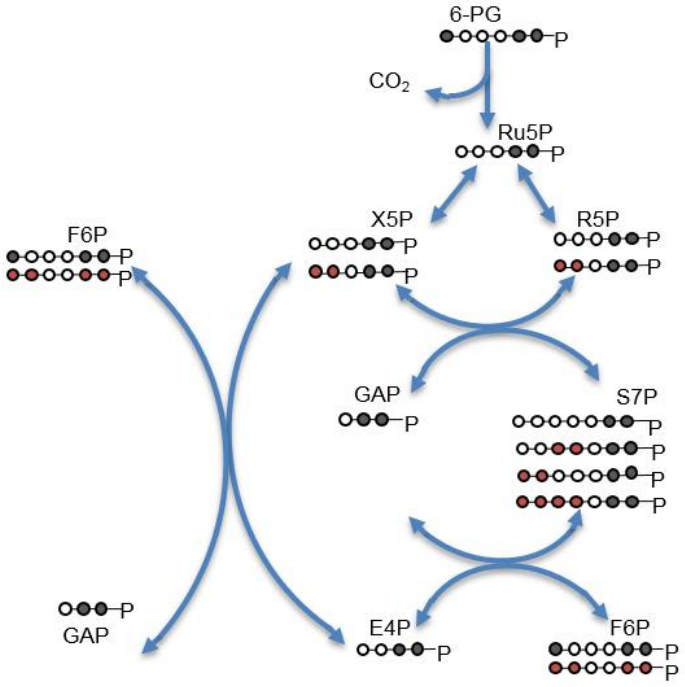

Fig. 15: Schematic representation of ^{13}C-labeled metabolites in PP pathway when grown on [1,5,6-$^{13}C_3$]-glucose and unlabeled benzoate. Metabolite abbreviations are the same as in Fig 1.

Fig. 16: The isotopic labeling fractions, with standard deviations, for six intracellular metabolites in the PP pathway when grown on [1,5,6-$^{13}C_3$]-glucose and unlabeled benzoate under Fe-limitation at $O.D_{600}$ 0.4 and 0.8. Metabolite abbreviations are the same as in Fig 1.

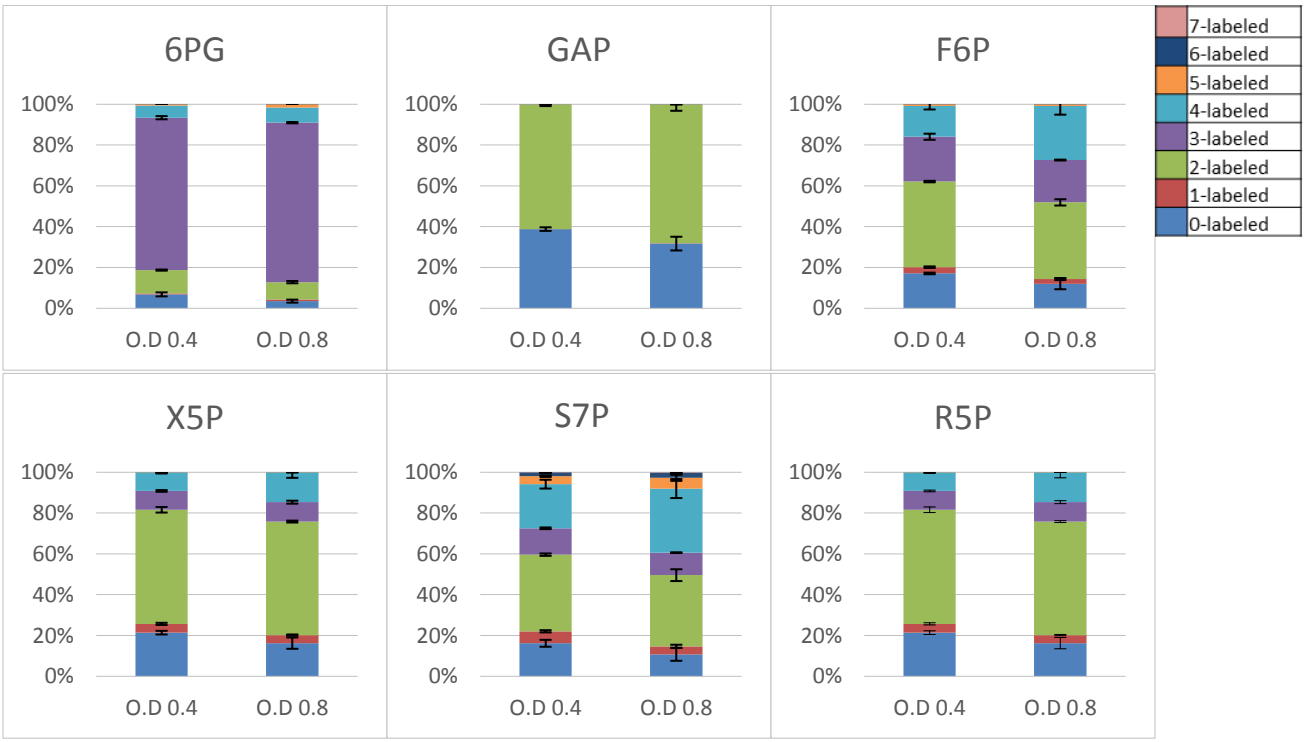

Fig. 17: The isotopic labeling fractions, with standard deviations, for six intracellular metabolites in the PP pathway when grown on [1,5,6-$^{13}C_3$]-glucose and unlabeled benzoate during first phase of Fe-starvation at $O.D_{600}$ 0.4 and 0.8. Metabolite abbreviations are the same as in Fig 1.

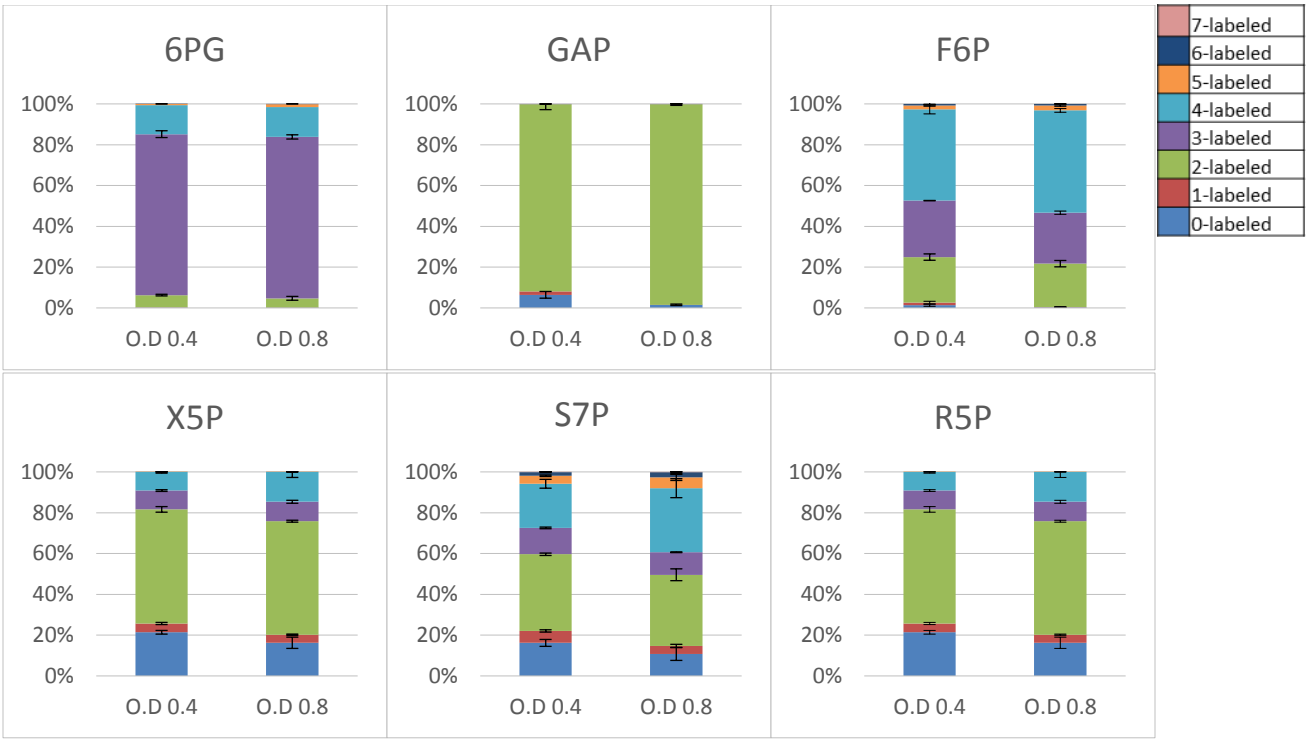

Fig. 18: The isotopic labeling fractions, with standard deviations, for six intracellular metabolites in the PP pathway when grown on [1,5,6-$^{13}C_3$]-glucose and unlabeled benzoate during second phase of Fe-starvation at $O.D_{600}$ 0.4 and 0.8. Metabolite abbreviations are the same as in Fig 1.

We then proceeded to monitor the assimilation of carbons through the TCA cycle. During the first phase of Fe-starved growth, the non-labeled fraction of pyruvate (84.5 ± 8.1%) and PEP (89.1 ± 1.9%) was significantly higher than the non-labeled fractions of pyruvate and PEP in Fe-limited (12.1±3.1% and 59.3±4.4%, respectively) and second phase of Fe-starved growth (39.5 ± 8.8% and 9.4 ± 0.0%, respectively) (Fig. 20, 21 and 22). This indicated a higher gluconeogenic flux from TCA cycle metabolites in the first phase of Fe-starved growth. During the second phase of Fe-starved growth, the ^{13}C-labeling patterns of metabolites were consistent with the canonical routing of carbons through the TCA cycle (Fig. 19). The anapleurotic reactions through the carboxylation of pyruvate and PEP (incorporating either non-labeled or singly ^{13}C-labeled carbon dioxide) would produce the same labeling patterns as described above for PEP and pyruvate without or with one extra ^{13}C-labeled carbon (Fig. 20, 21 and 22). Accordingly,

OAA (through aspartate) was determined to be 48.8 ± 9.0% non-labeled, 24.7 ± 3.0% singly, 21.6 ± 2.1% doubly, 4.3 ± 0.0% triply (Fig. 5). Decarboxylation of pyruvate produces non-labeled acetyl-CoA (from both non-labeled and singly and ^{13}C-labeled pyruvate) and doubly ^{13}C-labeled acetyl-CoA (from doubly ^{13}C-labeled pyruvate) (Fig. 19). The labeling pattern of citrate (38.1 ± 0.5% non-labeled, 22.7 ± 0.6% singly, 25.4 ± 0.2% doubly, 9.0± 0.5% triply, and 4.0 ± 0.4% quadruply ^{13}C-labeled) was consistent with the combination of acetyl-CoA with OAA (Fig. 5). Subsequent decarboxylation of citrate produced α-KG (48.75 ± 3.8 % non-labeled, 20.9 ± 0.0% singly, 21.6 ± 2.1% doubly, 6.0 ± 0.0% triply, and 2.2 ± 0.0% quadruply ^{13}C-labeled) (Fig. 22). The labeling pattern of fumarate (80.4 ± 2.2% non-labeled, 11.1 ± 0.0% singly, 8.0 ± 0.2% doubly) was consistent with the occurrence of another decarboxylation step between α-KG to produce succinate, the direct precursor to fumarate (Fig. 22). In Fe-limited and phase one Fe-starved cells, the influx of carbons from benzoate catabolism via the *ortho* pathway was greater. We take note that the similarity between labeling patterns of citrate and OAA indicated that the acetyl moiety in acetyl-CoA originated exclusively from benzoate (Fig. 19). In the Fe-limited cells, Citrate (80.6± 0.4% non-labeled, 11.9 ± 0.6% singly, and 5.6 ± 0.2% doubly ^{13}C-labeled) was produced from combining the non-labeled acetyl moiety with OAA (83.9 ± 0.3% non-labeled, 9.3 ± 0.4% singly, and 5.3 ± 0.3% doubly ^{13}C-labeled) (Fig. 5). The continuing TCA cycle metabolites were primarily non-labeled for both Fe-limited and phase 1 Fe-starved cells: non-labeled α-KG at 89.5 ± 0.8% and 96.9 ± 0.1% respectively, non-labeled fumarate at 99.9 ± 0.0% and 96.9 ± 0.1 respectively, and finally, non-labeled OAA at 84.9 ± 0.3% and 99.0 ± 0.2%, respectively (Fig. 20, 21 and 22).

Long-term isotopic enrichment of intracellular enabled us to map out the metabolic network. We further applied a MFA approach to quantify the carbon fluxes through the series of metabolic reactions in the cellular network generated above.

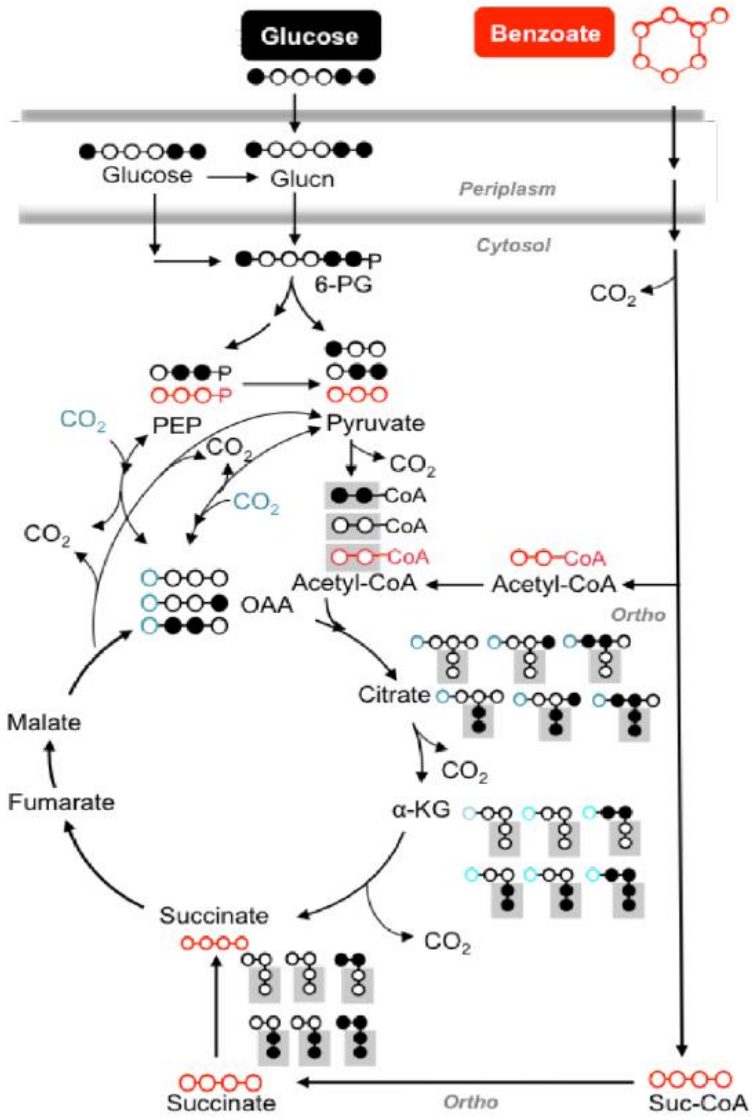

Fig. 19: Schematic representation of ^{13}C-labeled metabolites in the TCA cycle when grown on [1,5,6-$^{13}C_3$]-glucose and unlabeled benzoate. Metabolite abbreviations are the same as in Fig 1 (Kukurugya, 2017).

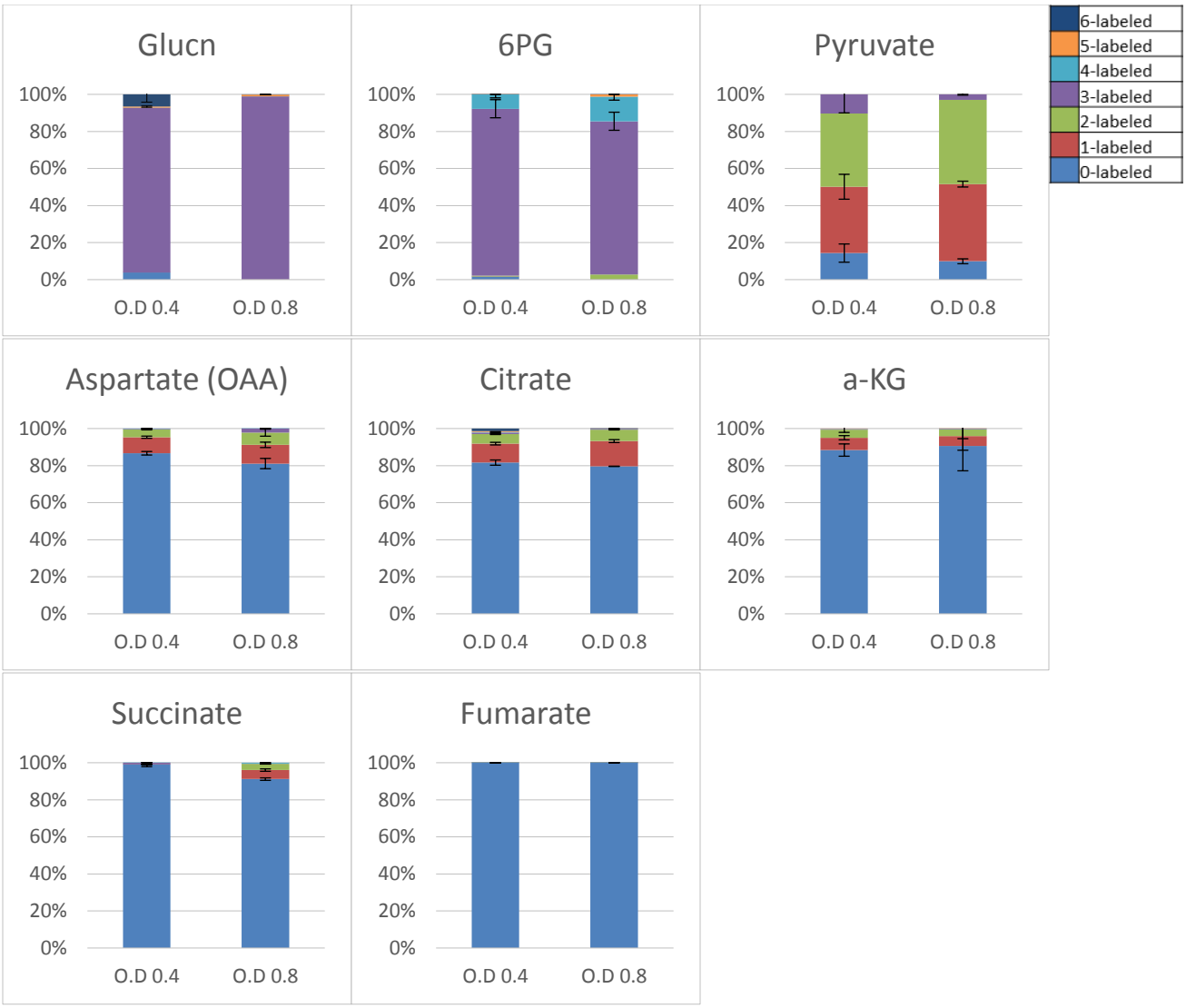

Fig. 20: The isotopic labeling fractions, with standard deviations, for eight intracellular metabolites in central carbon metabolism when grown on [1,5,6-$^{13}C_3$]-glucose and unlabeled benzoate under Fe-limitation at $O.D_{600}$ 0.4 and 0.8. Metabolite abbreviations are the same as in Fig 1.

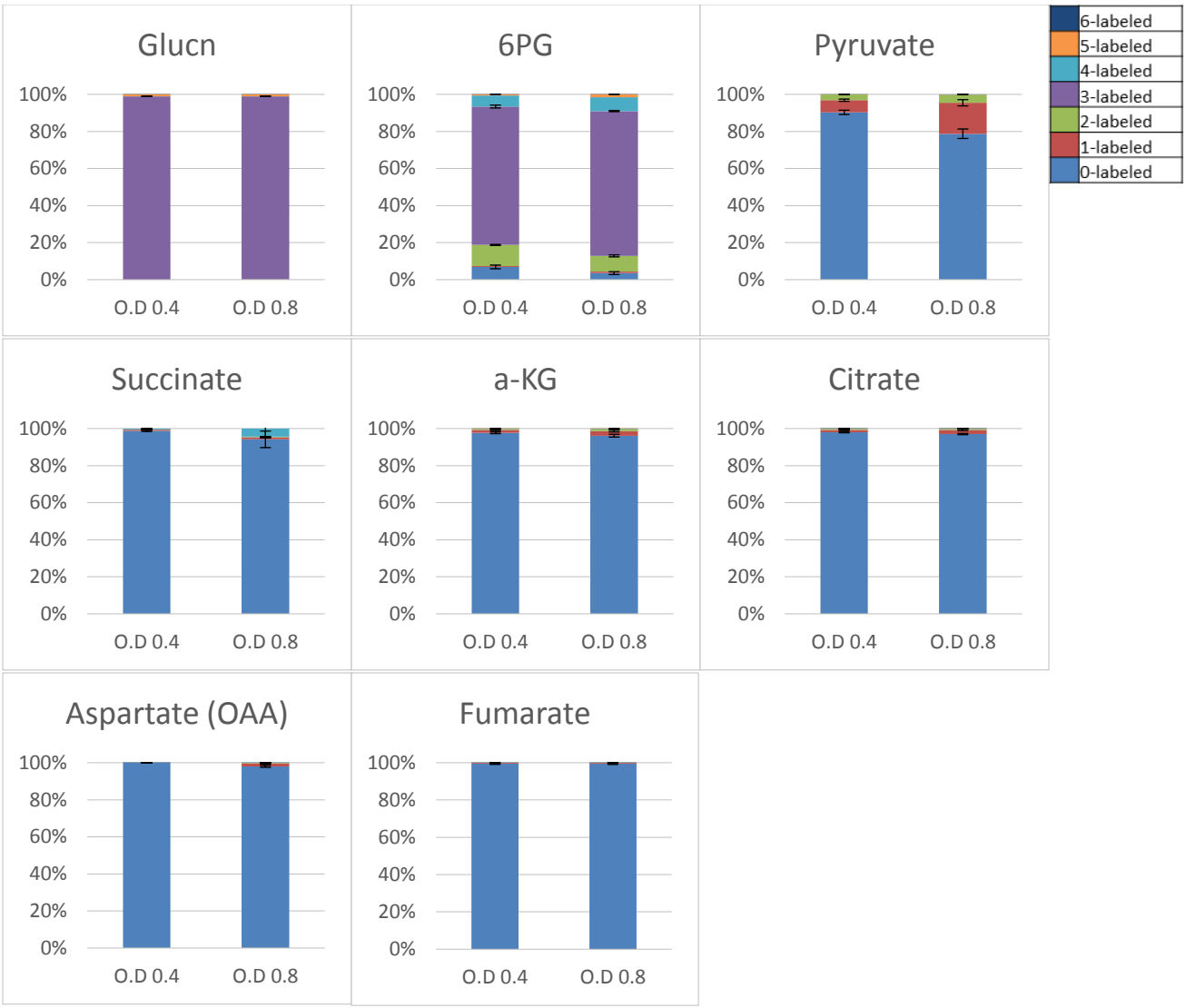

Fig. 21: The isotopic labeling fractions, with standard deviations, for eight intracellular metabolites in central carbon metabolism when grown on [1,5,6-$^{13}C_3$]-glucose and unlabeled benzoate during first phase of Fe-starvation at $O.D_{600}$ 0.4 and 0.8. Metabolite abbreviations are the same as in Fig 1.

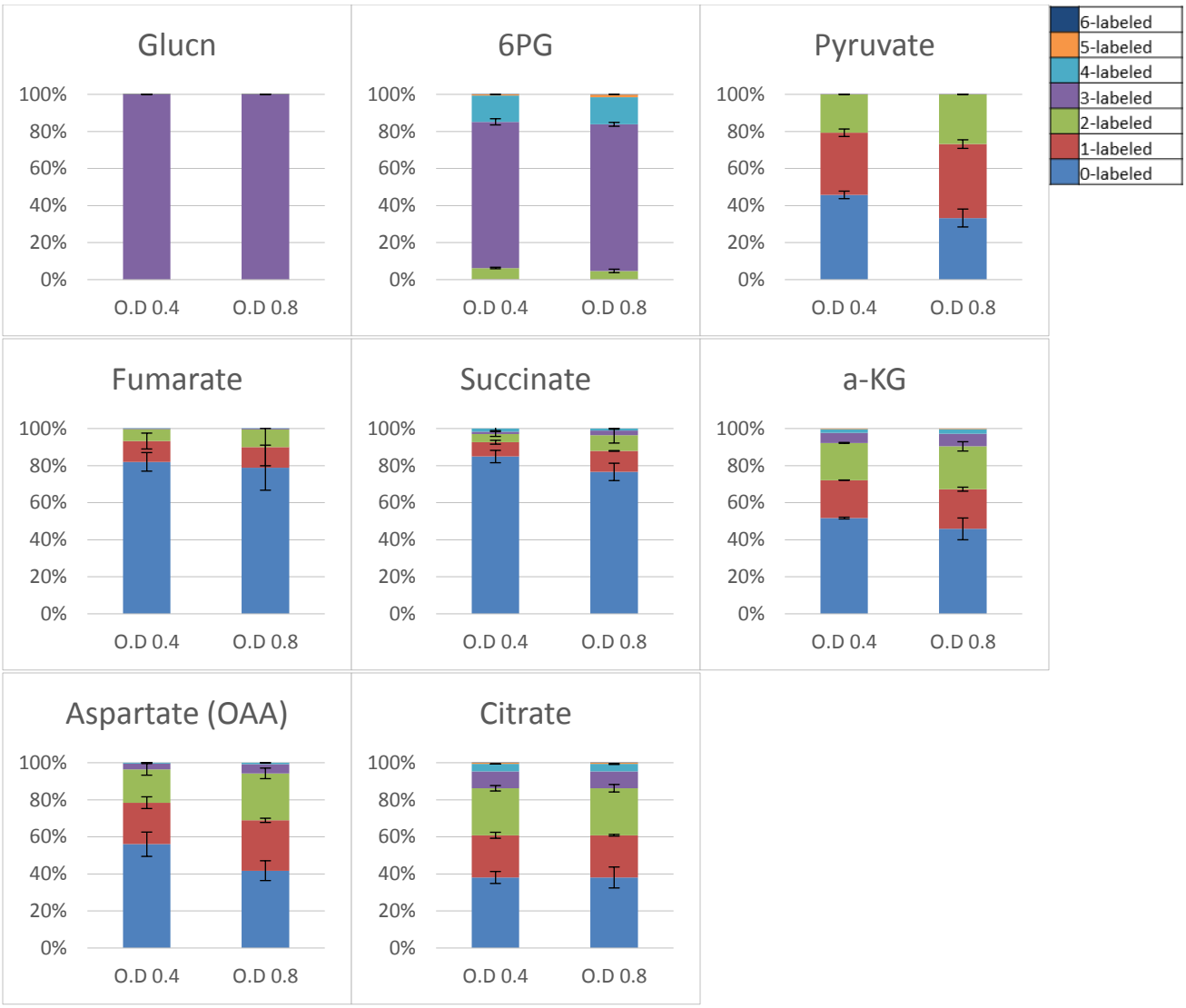

Fig. 22: The isotopic labeling fractions, with standard deviations, for eight intracellular metabolites in in central carbon metabolism when grown on [1,5,6-$^{13}C_3$]-glucose and unlabeled benzoate during second phase of Fe-starvation at $O.D_{600}$ 0.4 and 0.8. Metabolite abbreviations are the same as in Fig 1.

3.3 Siderophore Production

As siderophores are well-known to be metabolite expensive, we obtained the siderophore secretion rate. *P. putida* KT2440 does not secrete other specialized siderophores in addition to PVD (Cornelis 2010). For the Fe-limited cells, we measured a PVD secretion rate of 47.65±13.46 µmol g_{CDW}^{-1} h^{-1} (Fig. 23). It has been previously determined that a total of 62 moles of carbon was consumed from the central carbon metabolism to produce each mole of PVD (Sasnow et al., 2016; Wei and Aristilde, 2014; Schalk and Guillon 2013). Hence, the carbon equivalent secretion rate was measured to be 2.95±0.83 mmol C g_{CDW}^{-1} h^{-1} (Fig 5). For the Fe-starved condition, the siderophore production rate was measured to be 4.67±0.4 mmol C g_{CDW}^{-1} h^{-1} during the first phase. We note here the increase in the production of siderophores as a function of Fe limitation. However, in the second phase, the siderophore production decreased and was measured at 1.36±0.01 mmol C g_{CDW}^{-1} h^{-1}. Interestingly, this is in accordance with cells grown exclusively on glucose, quantified at 1.47±0.27 mmol C g_{CDW}^{-1} h^{-1} (Sasnow et al., 2016) (Fig 5). This could be due to the diauxic trend of growth in the Fe-starved cultures leading to the consumption of glucose as the primary substrate. We also note that our findings were consistent with previous work (Joshi et al., 2014) that implied an increased siderophore production in *Pseudomonas* cells grown on aromatic substrates.

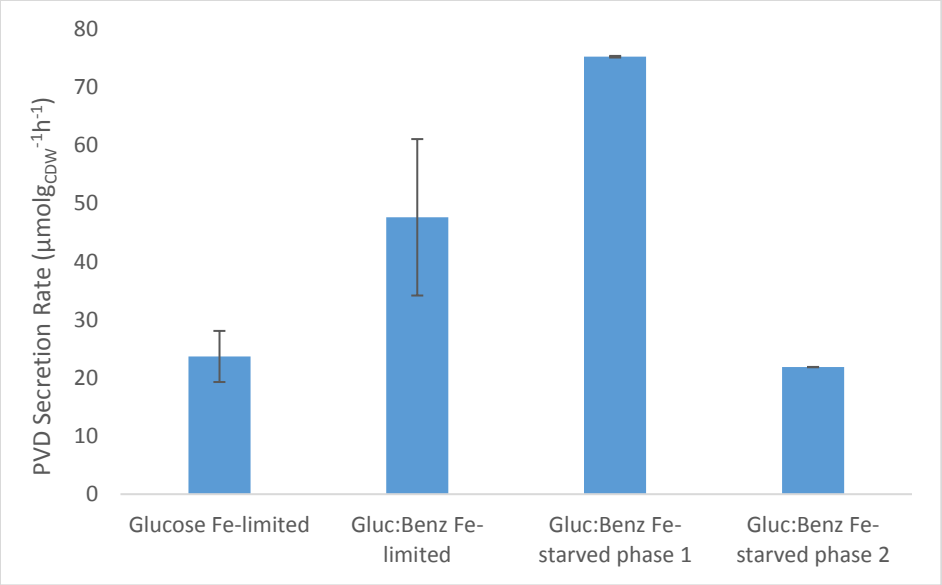

Fig 23: PVD secretion rates (µmolg$_{CDW}^{-1}$h^{-1}) for *P. putida* KT2440 cells grown on Fe-limited and Fe-starved glucose:benzoate and on Fe-limited glucose (Sasnow et al, 2016) medium.

3.4 Metabolic Flux Analysis

In order to determine the relative contributions of the different metabolic reactions in the Fe-replete and Fe-limited cells, we applied an MFA approach to quantitate the fluxes through various metabolic pathways. In addition to the steady-state ^{13}C-labeling experiments with [1,5,6 $^{13}C_3$]-glucose and unlabeled benzoate, our MFA was constrained using experimentally-determined substrate consumption rates, metabolite excretion rates, siderophore secretion rate and biomass growth. The agreement between model-estimated and experimentally-determined labeling patterns confirmed the good quality of the optimization fits for modeling the carbon metabolism in cells grown on Fe-replete and Fe-limited conditions. The normalized reactions rates (ratio of metabolic reaction rates over the composite substrate uptake rate) were determined (Fig. 24 and Table 1). In the Fe-replete and Fe-limited model, the normalized uptake rates for glucose uptake (44.2 ± 1.8% and 47.8 ± 20.3 %, respectively) and benzoate uptake (55.8 ± 1.7% and 52.23 ± 6.1%) were consistent with the relative fraction of the experimentally-determined values for substrate consumption (42.1 ± 9.4% and 42.8 ± 19.3%, respectively for glucose; and 57.9 ± 17.2% and 57.1 ± 4.0 %, respectively for benzoate) (Fig. 24 and Table 1).

For the Fe-replete and Fe-limited models, the MFA revealed similar fractional ratio of the total glucose uptake rate that was subjected to oxidation to gluconate (36.8 ± 1.3 % and 37.9 ± 2.3%, respectively). However, Fe-limited cells revealed a slight increase in the fraction of periplasmic glucose that was subjected to phosphorylation to G6P (11.7 ± 5.3%) when compared to the Fe-replete model (7.4 ± 0.5 %). Interestingly, the MFA also revealed that despite being under Fe-limitation, the metabolic fluxes across the ED pathway and reverse EMP pathway were not significantly impacted, and were in close agreement with the Fe-replete model. This was indicated by the similarity in the fluxes of 6-PG to pyruvate and GAP (41.8 ± 1.4 %), GAP to

DHAP (15.9 ± 0.6 %), DHAP and GAP to FBP (6.1 ± 1.2 %), FBP to F6P (12.1 ± 2.5%) and F6P to G6P (4.1 ± 0.8%) when cells were grown on the Fe-replete medium compared to cells grown on Fe-limited medium (43.3 ± 16.0 %, 23.3 ± 9.2 %, 7.7 ± 5.0 %, 15.1 ± 9 %, and 4.2 ± 1.7%, correspondingly) (Fig. 24 and Table 1). However, the flux from GAP to 3-PG was significantly reduced in the Fe-limited (4.06 ± 0.3 %) cells when compared to Fe-replete cells (12.2 ± 1.1 %). The flux from 3-PG to PEP remained the same across both conditions, but the flux from PEP to pyruvate was also reduced in the Fe-limited cells (3.8 ± 2.1 %) when compared to Fe-replete cells (17.9 ± 2.9 %). This was consistent with the Fe-limited behavior of glucose-grown cells (Sasnow et al., 2016).

Furthermore, the investment of carbon into the PP pathway was marginally increased in the Fe-limited cells (4.1 ± 1.4 %) when compared to Fe-replete cells (2.1 ± 0.0 %). This could potentially be due to the demand of PPP metabolites towards siderophore production in the Fe-limited cells. Under both conditions, the flux from Glucn to 2-Keto-Glucn was in close agreement with the flux from 2-Keto-Glucn to 6-PG, indicating a negligible excretion rate of 2-Keto-Glucn (0.05 ± 0.0 % for Fe-replete cells and 0.06 ± 0.0% for Fe-limited cells) (Table 1). As reported by Kukurugya (2017), our model also revealed that 6-PG was primarily derived from Glucn and 2-Keto-Glucn, and only secondarily derived from G6P. This was indicated by the lower flux of G6P to 6-PG (9.4 ± 0.0 % for Fe-replete and 11.9 ± 5.1 % for Fe-limited cells) when compared to the total flux of Glucn and 2-Keto-Glucn towards 6-PG (approximately 34.7 % for Fe-replete cells and 44.7 % for Fe-limited cells).

In the TCA cycle, the MFA results confirmed the participation of the glyoxylate shunt across both conditions (57.7 ± 7.6 % in Fe-replete cells and 53.5 ± 5.2 % in Fe-limited cells). Notably, the flux from succinate to fumarate (127.9 ± 8.3 %), fumarate to malate (128.9 ± 8.2

%), and malate to OAA (104.3 ± 3.5 %) was higher in the Fe-replete cells as compared to the Fe-limited cells (116.6 ± 5.2, 117.4 ± 4.0 %, and 90.9 ± 5.1 %, respectively) (Fig. 24). This was also in agreement with glucose grown Fe-limited cells (Sasnow et al., 2016).

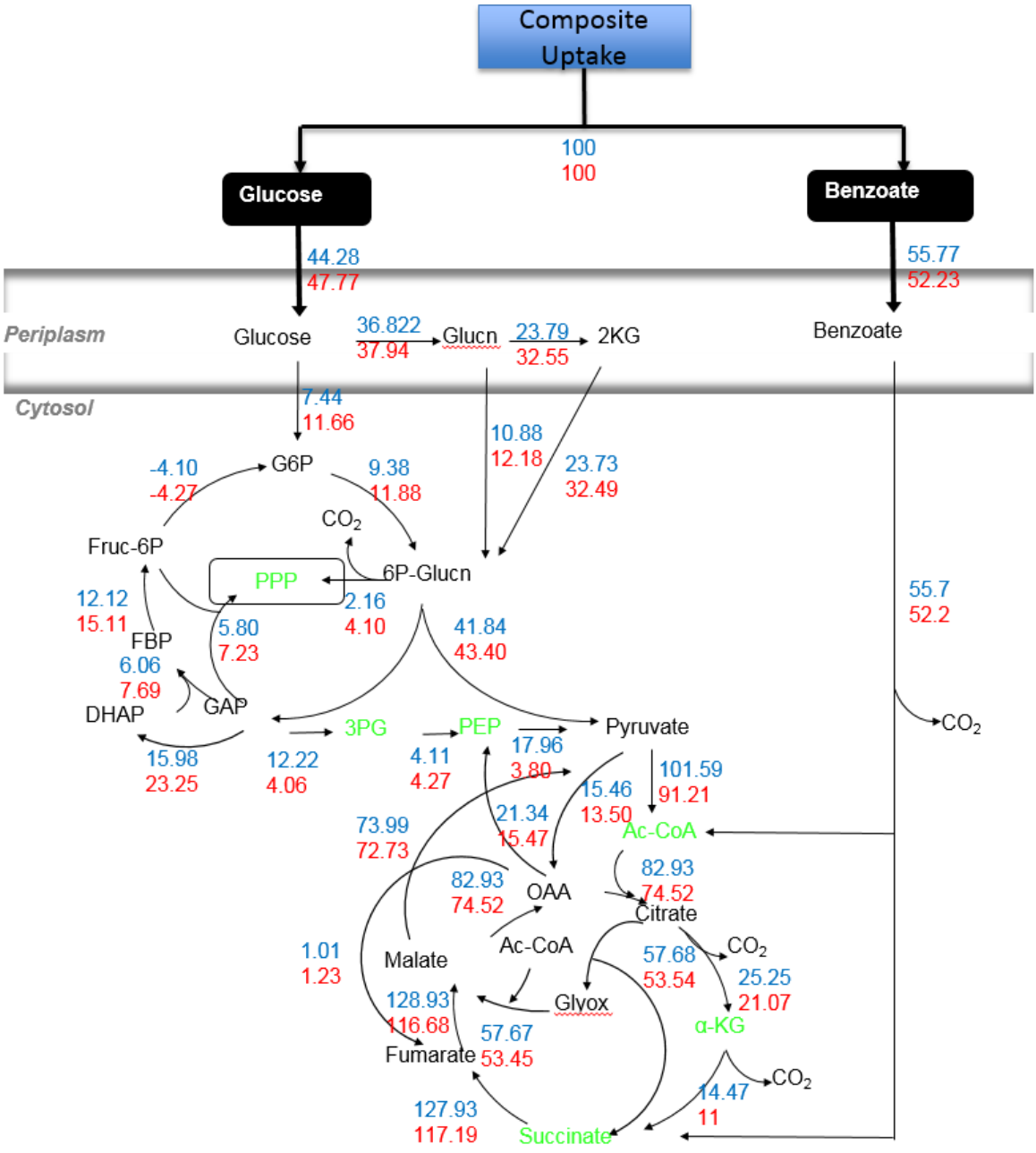

Fig 24: Metabolic flux analysis of Fe-replete Glucose:Benzoate. Abbreviations are as listed above. The MFA output of each metabolic reaction, the flux value, and the standard deviation of the flux value normalized to the Glucose:Benzoate consumption rate. The color blue and red represent the metabolic reaction rates (normalized to the composite uptake rate) of the Fe-replete and Fe-limited cells, respectively. Metabolites labeled green are involved in siderophore biosynthesis.

Table 1. The MFA output of each metabolic reaction, the flux value, and the standard deviation of the flux value normalized to the composite consumption rate. The reactions and fluxes shown in red are either secretions or biomass effluxes from the identified node. The values in blue represent the values seen in Fig. 8.

	Fe-Replete		Fe-limited	
Reaction	Flux Value (%)	Standard Dev (%)	Flux Value (%)	Standard Dev (%)
BM_AKG	10.77	0.23	10.07	0.01
BM_E4P	3.57	0.22	3.58	0.00
BM_OAA	14.49	0.29	13.18	0.57
BM_PEP	7.49	0.24	7.38	0.00
BM_PG3	8.11	0.34	8.22	0.00
BM_PYR	16.74	0.76	15.22	1.16
BM_R5P	2.70	0.16	2.70	1.16
Ex_AcCoA	16.76	0.64	15.48	1.02
Ex_DHAP	3.87	1.93	8.10	0.00
Ex_F6P	0.00	0.00	0.00	0.00
Ex_G6P	2.14	0.04	2.22	0.00
Ex_Glucn	2.15	0.04	2.25	0.00
Ex_KG2	0.05	0.00	0.06	0.00
Ex_Mal	8.31	0.33	7.72	0.53
Ex_S7P	4.29	1.97	6.16	7.83
Ex_X5P	1.13	0.50	3.62	2.52
Glucn->2KG	23.79	0.93	32.55	0.00
2KG->6PG	23.74	0.93	32.49	0.00
OAA->Fum	1.00	0.00	1.23	0.75
Mal->Pyr+CO2	74.00	12.67	72.73	5.31
G6P->6PG	9.38	0.05	11.88	5.34
6PG->Pyr + GAP	41.84	1.37	43.40	16.26
G6P->F6P	-4.10	0.50	-4.27	2.63
FBP->DHAP+GAP	-6.06	1.25	-7.46	4.01
GAP->PG3	12.22	1.13	4.06	0.27
PG3->PEP	4.11	0.79	4.29	0.46
PEP->Pyr	17.96	2.90	3.80	2.94
DHAP->GAP	-15.99	0.58	-23.25	9.29
Glucperi->Glucn	36.82	1.28	37.94	23.06
DHAP+GAP->FBP	6.06	1.25	7.69	5.29

FBP->F6P	12.12	2.51	15.15	9.30
Cit->Glx+Succ	57.68	7.61	53.45	5.23
Glx+AcCoA->Mal	57.68	7.61	53.45	5.23
Benz->AcCoA+Succ	55.77	1.65	52.23	6.05
X5P+R5P->GAP+S7P	2.07	0.36	3.34	0.70
GAP+S7P->E4P+F6P	-2.22	1.61	-3.65	5.96
E4P+Xu5P->F6P+GAP	-5.80	1.39	-7.23	5.96
Ru5P->X5P	1.05	0.53	-1.11	1.57
Ru5P->R5P	1.08	0.53	5.21	3.03
6PG->Ru5P	2.16	0.00	4.10	1.46
Pyr->AcCoA+CO2	101.59	11.68	91.21	12.72
Pyr+CO2->OAA	15.46	0.20	13.50	0.00
OAA->PEP+CO2	21.34	2.34	15.47	3.40
OAA+AcCoA->Citrate	82.93	6.37	74.52	0.43
Citrate->aKG	25.25	1.23	21.07	4.80
aKG->Succ+CO2	14.48	1.00	11.00	4.80
Succ->Fum	127.93	8.26	116.68	5.10
Fum->Mal	128.93	8.25	117.90	4.80
Mal->OAA	104.31	3.54	90.90	5.14
Gluc->Glucperi	44.23	1.77	47.77	20.34
CO2out->CO2	46.88	0.03	40.70	11.73
Glucperi->G6P	7.42	0.51	11.66	5.31
Glucnperi->6PG	10.88	0.39	12.18	10.26
Benz->Benzperi	55.77	1.65	52.23	6.05

Table 2. The metabolic flux values from the MFA. The units for the Average value and the Standard deviation are (mmol g_{CDW}^{-1} h^{-1}).

	Fe-replete		Fe-limited	
Reaction	Av. (mmol g_{CDW}^{-1} h^{-1})	Std. Dev.	Av. (mmol g_{CDW}^{-1} h^{-1})	Std. Dev.
BM_AKG	0.84	0.02	1.31	0.00
BM_E4P	0.28	0.02	0.46	0.00
BM_OAA	1.13	0.02	1.71	0.07
BM_PEP	0.58	0.02	0.96	0.00
BM_PG3	0.63	0.03	1.07	0.00
BM_PYR	1.31	0.06	1.98	0.15
BM_R5P	0.21	0.01	0.35	0.15
Ex_AcCoA	1.31	0.05	2.01	0.13
Ex_DHAP	0.30	0.15	1.05	0.00
Ex_F6P	0.00	0.00	0.00	0.00
Ex_G6P	0.17	0.00	0.29	0.00
Ex_Glucn	0.17	0.00	0.29	0.00
Ex_KG2	0.00	0.00	0.01	0.00
Ex_Mal	0.65	0.03	1.00	0.07
Ex_S7P	0.33	0.15	0.80	1.02
Ex_X5P	0.09	0.04	0.47	0.33
Glucn->2KG	1.86	0.07	4.22	0.00
2KG->6PG	1.85	0.07	4.22	0.00
OAA->Fum	0.08	0.00	0.16	0.10
Mal->Pyr+CO2	5.78	0.99	9.44	0.69
G6P->6PG	0.09	0.00	1.54	0.69
6PG->Pyr + GAP	3.27	0.11	5.63	2.11
G6P->F6P	-0.32	0.04	-0.55	0.34
FBP->DHAP+GAP	-0.47	0.10	-0.97	0.52
GAP->PG3	0.95	0.09	0.53	0.04
PG3->PEP	0.32	0.06	0.56	0.06
PEP->Pyr	1.40	0.23	0.49	0.38
DHAP->GAP	-1.25	0.05	-3.02	1.21
Glucperi->Glucn	2.87	0.10	4.92	2.99
DHAP+GAP->FBP	0.47	0.10	1.00	0.69
FBP->F6P	0.95	0.20	1.97	1.21
Cit->Glx+Succ	4.50	0.59	6.94	0.68

Glx+AcCoA->Mal	4.50	0.59	6.93	0.68
Benz->AcCoA+Succ	4.35	0.13	6.78	0.79
X5P+R5P->GAP+S7P	0.16	0.03	0.43	0.09
GAP+S7P->E4P+F6P	-0.17	0.13	-0.47	0.77
E4P+Xu5P->F6P+GAP	-0.45	0.11	-0.94	0.77
Ru5P->X5P	-0.20	0.04	-0.14	0.20
Ru5P->R5P	0.37	0.04	0.68	0.39
6PG->Ru5P	0.17	0.00	0.53	0.19
Pyr->AcCoA+CO2	7.93	0.91	11.84	1.65
Pyr+CO2->OAA	1.21	0.02	1.75	0.00
OAA->PEP+CO2	1.67	0.18	2.01	0.44
OAA+AcCoA->Citrate	6.47	0.50	9.67	0.06
Citrate->aKG	1.97	0.10	2.73	0.62
aKG->Succ+CO2	1.13	0.08	1.43	0.62
Succ->Fum	5.09	0.00	15.14	0.73
Fum->Mal	10.06	0.64	15.30	0.63
Mal->OAA	8.14	0.28	11.80	0.67
Gluc->Glucperi	3.45	0.14	6.20	2.64
CO2out->CO2	3.66	0.00	5.28	1.52
Glucperi->G6P	0.58	0.04	1.51	0.69
Glucnperi->6PG	0.85	0.03	1.58	1.33
Benz->Benzperi	4.35	0.13	6.78	0.79

4. CONCLUDING REMARKS

Here we employed a stable isotope-assisted metabolomics and MFA to unravel the consequences of Fe-limitation on the metabolism of mixed substrates by a model soil bacterium of biotechnological importance, *Pseudomonas putida* KT2440. It has already been established that this bacterium can utilize both sugars and aromatic substrates simultaneously. The focus of this study was to elucidate the Fe-dependent cellular reprogramming of mixed-substrate metabolism.

Our work revealed several findings that contribute to a better understanding of nutrient-dependent carbon metabolism. First, we report that the Fe-limitation did not affect biomass growth of the cells, but instead, caused an overall increase in substrate consumption coupled with secretion of the pyoverdine siderophore. Second, with the increase in the extent of Fe-limitation, we found an increase in the preferential intake of the aromatic substrate. In the condition with the lowest bioavailable Fe, the growth was divided across two phases, wherein the aromatic substrate was consumed in the first phase, followed by the sugar in the second phase. This validated our hypothesis that the increase in the preferential intake of the aromatic substrate was due to its favorability in the production of siderophores. Third, it was evident that the glucose-derived carbons mainly populated the ED and reverse EMP pathways whereas benzoate-derived carbons dominated the TCA and glyoxylate cycles across all conditions. However, under Fe-limitation and Fe-starvation, we found that benzoate was minimally incorporated into G6P, DHAP, FBP and F6P.

For the further directions of this project, additional MFA models for each phase of the diauxic growth in the Fe-starvation condition would further elucidate the reprogramming of mixed substrate metabolism in response to very low Fe availability. Additionally, kinetic flux

experiments for the mixed substrates under Fe-limitation and Fe-starvation could potentially shed light upon the *in vivo* changes in metabolic enzyme activity. Finally, using proteomic analysis for the Fe-replete and Fe-limited conditions to connect the elucidated changes in carbon fluxes to specific enzymatic regulation could aid in the determination of the level of regulation in *P.putida* KT2440 under Fe-limitation.

It is widely known that *P. putida* KT2440 is ubiquitous in soil environments. As the bioavailability of Fe in the environment is very low, and glucose and aromatics are present as either naturally occurring compounds or contaminants, this study poses a significant contribution towards a comprehensive understanding of the effects of Fe-limitation on mixed substrate metabolism in the environment. Furthermore, *P. putida* is extensively used for its biocontrol and bioremediation properties. The findings demonstrated in this study and the collective efforts mentioned above can in turn support the development of novel biotechnological applications in industrial bioengineering and bioremediation.

BIBLIOGRAPHY

Adour, L.; Couriol, C.; Amrane, A. Diauxic growth of *Penicillium camembertii* on glucose and arginine. 2005. Enzyme and microbial technology. 36: 198-202.

Amador-Noguez, D. *et al.* Systems-level metabolic flux profiling elucidates a complete, bifurcated tricarboxylic acid cycle in *Clostridium acetobutylicum*. Journal of Bacteriology. 192**,** 4452–4461 (2010).

Andrews, S.C.; Robinson, A. K.; Rodriguez-Quinones. Bacterial iron homeostasis. 2003. FEMS Microbiology Reviews. 27: 215-237.

Antoniewicz, M. R. 13C metabolic flux analysis: optimal design of isotopic labeling experiments. 2013. Current Opinion in Biotechnology. 24: 1116-1121.

Aristilde, L., Lewis, I. A., Park, J. O. & Rabinowitz, J. D. Hierarchy in Pentose Sugar Metabolism in *Clostridium acetobutylicum*. 2015. Applied Environmental Microbiology. 81: 1452–146.

Basu, A.; Apte, S. K.; Phale, P. S. Preferential Utilization of Aromatic Compounds over Glucose by *Pseudomonas putida* CSV86. 2006. Applied and Environmental Microbiology. 72: 2226-2230.

Basu, A.; Shrivastava, R., Basu, B., Apte, S.K., Phale, P.S. Modulation of glucose transport causes preferential utilization of aromatic amino compounds in *Pseudomonas putida* CSV86. Journal of Bacteriology. 2007, 189: 7556–7562.

Bollag, J.; Myers, C. J.; Minard, R. D. Biological and chemical interactions of pesticides with soil organic matter. 1992. Science of the Total Environment. 123: 205-217.
Boukhalfa, H.; Crumbliss, A. L. Chemical aspects of siderophore mediated iron transport. 2002. Biometals. 15: 325-339.

Bran, V.; Hantke, K. Recent insights into iron import by bacteria. 2011. Current Opinion in Chemical Biology. 15: 328-334.

Buescher, J.M.; Antoniewicz, M.R.; Boros, L.G.; Burgess, S.C.; Bruengraber, H.; Clish, C. B.; DeBeradinis, R.J.; Feron, O.; Frezza, C.; Ghesquiere, B.; Gottlieb, E.; Hiller, K.; Jones, R.G.; Kamphorst, J.J.; Kibbey, R. G.; Kimmelman, A. C.; Locasale, J. W.; Lunt, S. Y.; Maddocks, O. DK; Malloy, C.; Metallo, C. M.; Meuillet, E. J.; Munger, J.; Nöh, Katharina, Rabinowitz, J. D.; Ralser, M.; Sauer, U.; Stephanopoulos, G.; St-Pierre, J.; Tennant, D. A.; Wittmann, C.; Vander Heiden, M. G.; Vazquez, A.; Vousden, K.; Young, J. D.; Zamboni, N.; Fendt, S. A roadmap for interpreting ^{13}C metabolite labeling patterns from cells. Current Opinion in Biotechnology. 2015. 34: 189-201.

Cao, B.; Loh, K. Catabolic pathways and cellular responses of *Pseudomonas putida* P8 during growth on benzoate with a proteomics approach. Biotechnology and Bioengineering. 2008. 101: 1297-1312.

Chavarría, M.; Nikel, P.; Pérez-Pantoja, D.; de Lorenzo, V. The Entner-Doudoroff pathway empowers *Pseudomonas putida* KT2440 with a high stress tolerance to oxidative stress. 2013. Environmental Microbiology. 15:1772-785.

Crown, S. B.; Antoniewicz, M. R. Parallel labeling experiments and metabolic flux analysis: past, present and future methodologies. 2012. Metabolic Engineering. 16:21-32.

Fuhrer, T.; Fischer, E.; Sauer, U. Experimental identification and quantification of glucose metabolism in seven bacterial species. 2005. Journal of Bacteriology. 187: 1581-1590.

Gaines, G. L.; Smith, L.; Neidle, E. L. Novel nuclear magnetic resonance spectroscopy methods demonstrate preferential carbon source utilization by Acinetobacter calcoaceticus. 1996. J. Bacteriol. 178: 6833-6841

George, K. W.; Hay, A. Less is more: reduced catechol production permits Pseudomonas putida F1 to grow on styrene. 2012 Microbiology. 158: 2781-2788.

Kögel-Knabner, I. The macromolecular organic composition of plant and microbial residues as inputs to soil organic matter. 2002. Soil Biology and Biochemistry 34:139-162.

Kukurugya, M. A. 2017. Quantifying the intracellular metabolic network that establishes the simultaneous utilization of sugars and aromatic substrates in *Psuedomonas putida* KT 2440 (Unpublished master's thesis). Cornell University, Ithaca, NY.

La Rosa, R.; Nogales, J.; Rojo, F. The Crc/CrcZ-CrcY global regulatory system helps the integration of gluconeogenic and glycolytic metabolism in *Pseudomonas putida*. 2015. Environmental Microbiology. 17: 3362-378.

Moorhead, D. L.; Lashermes, G.; Sinsabaugh, R. L.; Weintraub, M. N. Calculating co-metabolic cost of lignin decay and their impacts on carbon use efficiency. 2013. Soil Biology and Biochemistry. 66: 17-19.

Nelson, K. E.; Weinel, C.; Paulsen, I. T.; Dodson, R. J.; Hilbert, H.; Martins dos Santos, V. A. P.; Fouts, D. E.; Gill, S. R.; Pop, M.; Holmes, M.; Brinkac, L.; Beanan, M.; DeBoy, R.T.; Daughtery, S.; Kolonay, J.; Madupu, R.; Nelson, W.; White, O.; Peterson, J.; Khouri, H.; Hance, I.; Chris Lee, P.; Holtzapple, E.; Scanlan, D.; Tran, K.; Moazzez, A.; Utterback, T.; Rizzo, M.; Lee, K.; Kosack, D.; Moestl, D.; Wedler, H.; Lauber, J.; Stjepandic, D.; Hoheisel, J.; Straetz, M.; Heim, S.; Kiewitz, C.; Eisen, J.; Timmis, K.N.; Düsterhöft, A.; Tümmler, B.; Fraser, C. M. Complete genome sequence and comparative analysis of the metabolically versatile *Pseudomonas putida* KT2440. Environ. Microbiol. 2002. 4: 799-808.

Nishimura, T.; Vertès, A. A.; Shinoda, Y.; Inui, M.; Yukawa, H. Anaerobic growth of Corynebacterium glutamicum using nitrate as a terminal electron acceptor. 2007. Applied Microbial and Cell Physiology. 75: 889-897.

Nikel, P.I; Chavarría, M.; Fuhrer, T.; Sauer, U.; de Lorenzo, V. Pseudomonas putida KT2440 strain metabolizes glucose through a cycle formed by enzymes of the entner-doudoroff, embden-meyerhof-parnas, and pentose phosphate pathways. 2015. The Journal of Biological Chemistry. 290: 25920-25932.

Park, J. O.; Rubin, S. A.; Xu, Y.; Amador-Noguez, D.; Fan, J.; Shlomi, T.; Rabinowitz, J.D. Metabolite concentrations, fluxes and free energies imply efficient enzyme usage. 2016. Nature Chemical Biology. 12:482-489.

Parween, M.; Ramanathan, A.L.; Khillare, P. S.; Raju, N. J. Persistence, variance and toxic levels of organochlorine pesticides in fluvial sediments and the role of black carbon in their retention. 2014. Environmental Science and Pollution Research. 21: 6525-6546.

Pietkäinen, J.; Pettersson, M.; Bååth, E. Comparison of temperature effects on soil bacterial and fungal growth rates. 2005. FEMS Microbiology Ecology. 75: 1589-96.

Sasnow, S.S., Wei, H., Aristilde, L. Bypass in intracellular glucose metabolism in iron-limited *Pseudomonas putida*. 2016. Microbiology Open. 1:3-20.

Sudarsan, S.; Blank, L.M.; Dietrich, A.; Vielhauer, O.; Takors, R.; Schmid, A.; Reuss, M. Dynamics of benzoate metabolism in *Pseudomonas putida* KT2440. Metabolic Engineering Communications. 3:97-110.

Sudarsan, S.; Dethlefsen, S.; Blank, L. M.; Siemann-Herberg, M., Schmid, A. The Functional Structure of Central Carbon Metabolism in *Pseudomonas putida* KT2440. 2014. Appl. Environ. Microbiol. 80:5292-5303.

Wang, C. H.; Stern, I. J.; Gilmour, C. M., The catabolism of glucose and gluconate in *Pseudomonas* species. 1959. Biochemical Biophysics. 81:489-492.

Wood, W. A. Carbohydrate oxidation by *Pseudomonas fluorescens*. 1954. Bacteriological Reviews. 206:625-635.

Worsey, M.J.; Williams, P.A. Metabolism of toluene and xylenes by *Pseudmonas putida* mt-2: evidence for a new function of the TOL plasmid. 1975. Journal of Bacteriology. 124: 7-13.

Appendix

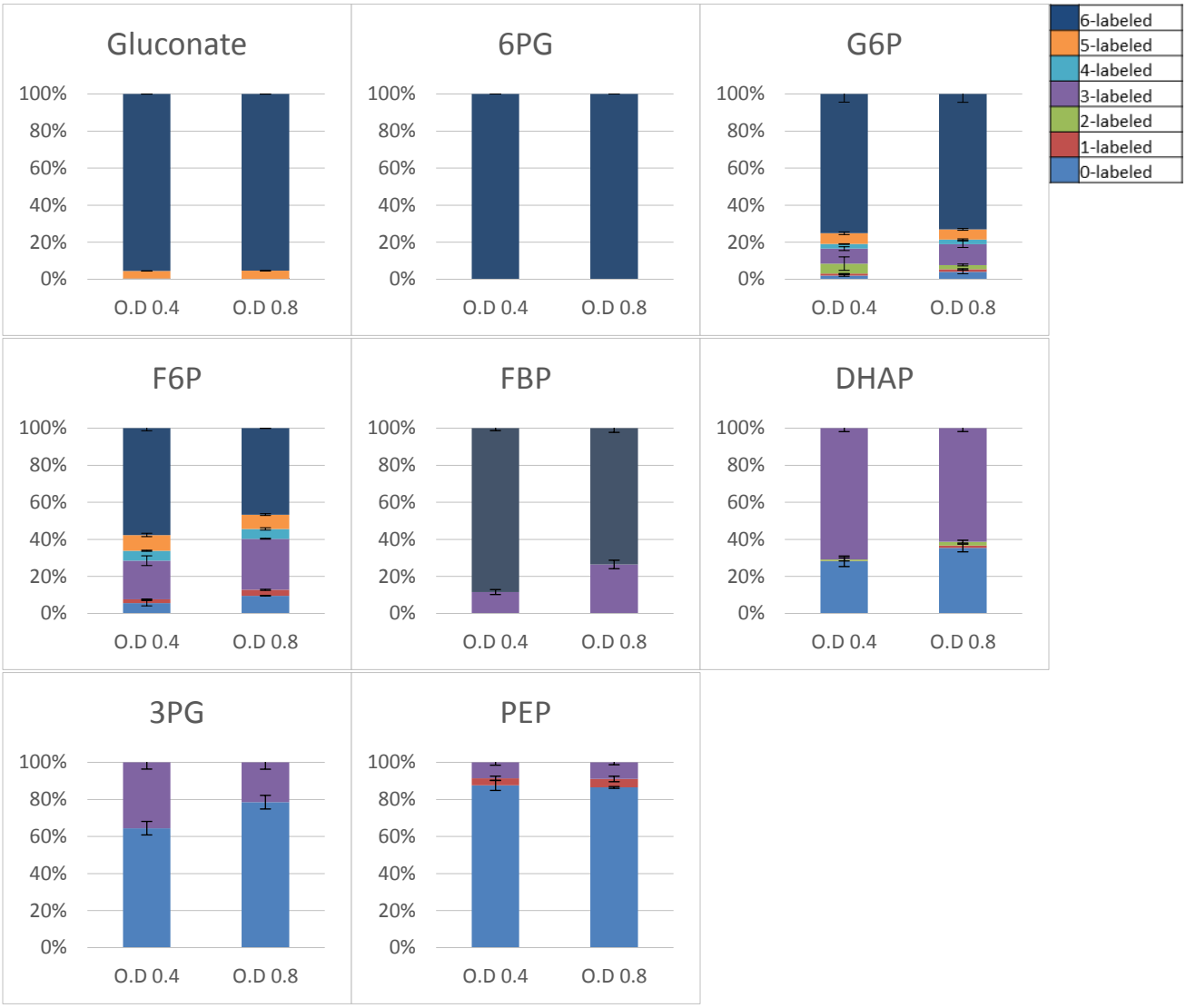

Figure S1. The isotopic labeling fractions, with standard deviations, for nine intracellular metabolites in the ED and EMP pathways when grown on [U-$^{13}C_6$]-glucose and unlabeled benzoate under Fe-limitation. Metabolite abbreviations are the same as in Fig 1.

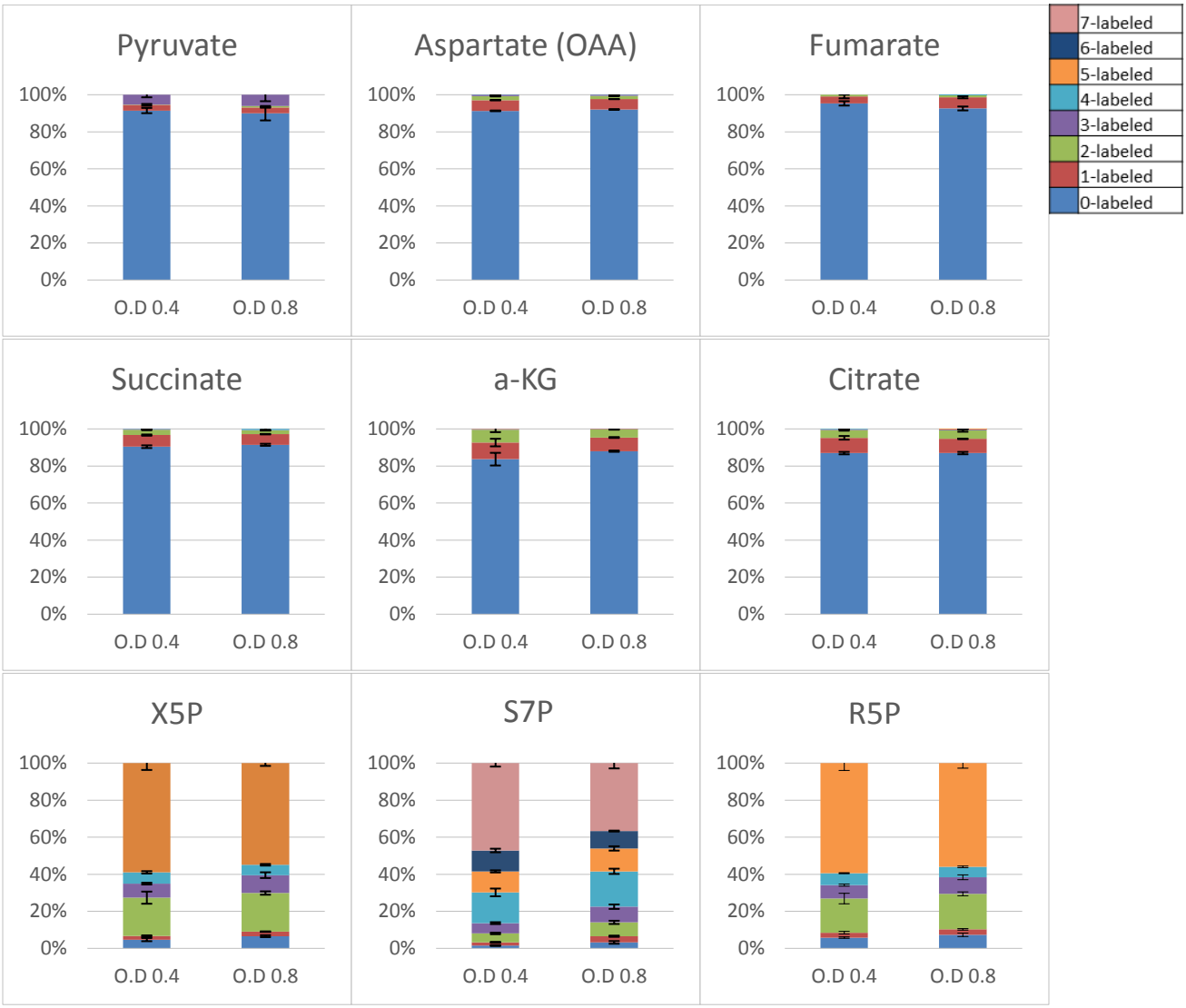

Figure S2. The isotopic labeling fractions, with standard deviations, for nine intracellular metabolites in the TCA cycle and PP pathway when grown on [U-$^{13}C_6$]-glucose and unlabeled benzoate under Fe-limitation. Metabolite abbreviations are the same as in Fig 1.

Figure S3. The isotopic labeling fractions, with standard deviations, for nine intracellular metabolites in the ED and EMP pathways when grown on [U-$^{13}C_6$]-glucose and unlabeled benzoate under Fe-starvation. Metabolite abbreviations are the same as in Fig 1.

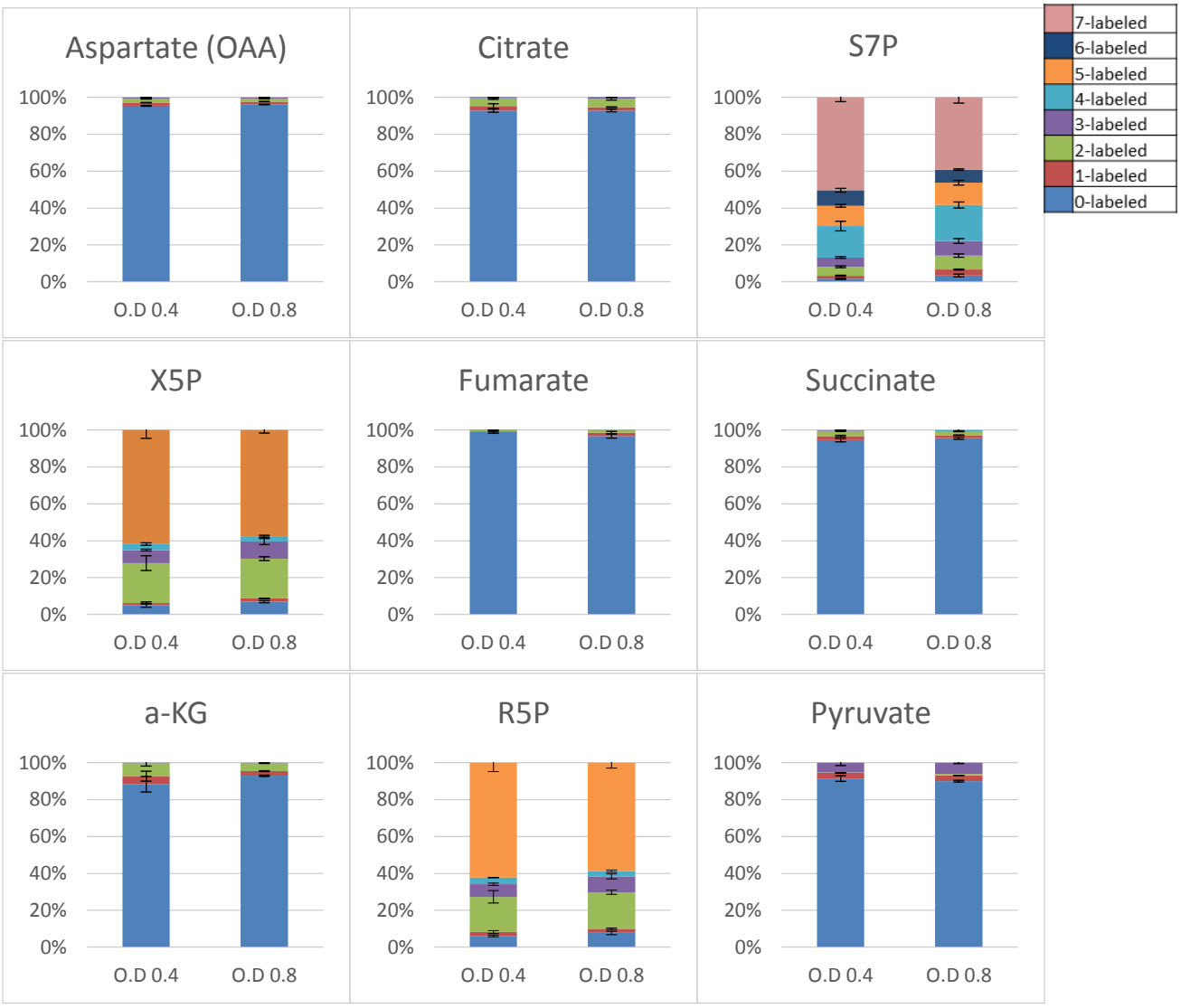

Figure S4. The isotopic labeling fractions, with standard deviations, for intracellular metabolites in the TCA cycle and PP pathway when grown on [U-$^{13}C_6$]-glucose and unlabeled benzoate under Fe-starvation. Metabolite abbreviations are the same as in Fig 1.